Department of Precision and Microsystems Engineering

DESIGN OF A SURFACE INSPECTION TOOL FOR RAPID DETECTION OF MICROMETER-SIZED WATER DROPLETS ON A SILICON WAFER

TIM VAN DRIEL

Report no	: 2022.023
Coach	: Dr.ir. L. Cacace
Professor	: Prof.dr.ir. J.L. Herder
Specialisation	: MSD/OM
Type of report	: MSc. Thesis
Date	: 04/07/2022

TU Delft Delft University of Technology

Challenge the future

Design of a surface inspection tool for rapid detection of micrometer-sized water droplets on a silicon wafer

MSc. Thesis

by

T. van Driel

to obtain the degree of Master of Science
at the Delft University of Technology,
to be defended publicly on Monday the 4th of July 2022 at 11:00

Committee:	Prof.dr.ir. J.L. Herder	TU Delft
	Dr.ir. L.A. Cacace	TU Delft
	Dr.ir. P. Blom,	VDL Enabling Technologies Group

An electronic version of this thesis is available at http://repository.tudelft.nl/.

TU Delft

Acknowledgements

I would like to use this section to sincerely thank the people who made this research possible. First I would like to thank Lennino Cacace and Paul Blom for their patience and thoughtfulness, due to various circumstances, this thesis has taken up much more time than anyone anticipated. Nevertheless they never became impatient - and always remained deeply involved in this project. Over the past year they have given me countless pieces of professional- and personal advise that I will benefit from for the rest of my life.

Lastly I wish to show my most sincere gratitude to Wim van Amstel. His volunatry involvement in this project has helped me tremendously. Not only did he supply me with optical components to perform my experiments - he invited me to his home, and granted me countless hours of his time to share his vast knowledge in the field of laser scanners with me. I can truly say that this project would not have been successful without your involvement.

Abstract

In this design study a new design is proposed for an in situ surface inspection tool that can rapidly detect micrometer sized water droplets on a silicon wafer. This surface inspection tool is part of a proposed redesign of the thermal conditioning stage of VDL-ETGs atmospheric wafer handler. A meticulous requirements study was performed, and the most important results were the following: 1) droplets with diameters larger than 35 µm should be measured, 2) the size, shape and location of the droplets is not relevant, 3) the wafer is not allowed to heat up by more than 3 mK as a result of the inspection, 4) the entire wafer surface should be inspected in less than 2 seconds and 5) only one droplet may pass undetected in every 6200 wafers. Several concepts were generated and after comparing them the synchronous dark-field flying spot scanner was selected, mainly for its high signal strength, and the low amount of signal fluctuation for different droplet locations. The design contains several parameters, the combination of which influence the system performance in a non-trivial way. A parametric design tool has been developed that takes in the design parameters as inputs, and outputs the system performance values and important design dimensions. This design tool was used to find design parameters that yield the desired performance. A simplified version of the design was built as an experimental setup for validation. For the experimental setup, a small spot size was chosen. This allowed us to better characterize the scattering behavior, however as a consequence this also prevented us from directly comparing the experimental results to the system performance yielding from the design tool. The experimental results were the following: 1) A very small part of the droplet surface is responsible for the large majority of the measured scattering, 2) the peaks are narrower in the cross-scan direction than in the scan direction, most likely due to the droplets being flat. 3) The measured noise is much higher than the predicted noise, this is likely due to poor grounding, poor shielding or a lack of filtering out high frequencies. Although the experimental setup yielded interesting results, the setup was not sufficient to fully validate the design – further experimentation is required to determine 1) if the predicted signal amplitude is correct, 2) if the signal amplitude scales with the square of the diameter of a droplet, 3) if the optical components remain as clean as we expect during operation of the dry unit, and 4) if the noise levels can be reduced to the desired level. Additionally, to improve the design further we suggest looking into ways of reducing the wafer warp and wobble.

Contents

1 Introduction 1
- 1.1 Wafer conditioning at VDL-ETG. 1
- 1.2 Project goal 2

2 Requirements 3
- 2.1 Summary tables. 3
- 2.2 Clarification. 4

3 Concept generation and selection 9
- 3.1 Detection principles 9
- 3.2 Light scattering 11
- 3.3 Performance criteria 12
  - 3.3.1 Discriminative power 13
  - 3.3.2 Measurement speed 13
  - 3.3.3 Effect on wafer temperature 13
- 3.4 Concepts 14
  - 3.4.1 Concept 1: Dark-field camera inspection 14
  - 3.4.2 Concept 2: Dark-field laser sheet scanner 15
  - 3.4.3 Concept 3: Synchronous dark-field flying-spot scanner 15
- 3.5 Concept selection. 15

4 First principles design 17
- 4.1 Design goals 17
  - 4.1.1 Quantifying discriminative power 17
  - 4.1.2 Quantifying wafer heating 19
  - 4.1.3 Quantifying measurement time 20
- 4.2 Gaussian beam propagation 20
- 4.3 Scanning geometry 21
  - 4.3.1 Scan lines, polygon duty cycle, scan angle and radial scan distance 21
  - 4.3.2 Spot size, pixel size, and bandwidth 22
- 4.4 Signal strength 23
  - 4.4.1 Incident light intensity. 23
  - 4.4.2 Scattering profile. 24
  - 4.4.3 Field of view to collection optics 25
- 4.5 Signal variation 26
  - 4.5.1 Illumination variation 26
  - 4.5.2 Field-of-view variation. 28
  - 4.5.3 Scattering profile variation. 28
- 4.6 Noise power. 28
- 4.7 Circular obstruction 29
- 4.8 Contamination of optical components 29
- 4.9 Parametric design tool 30
- 4.10 Design summary 32

5 Experimental validation 33
- 5.1 Goals experimental validation 33
- 5.2 Preliminary testing: Proof of concept 33
- 5.3 Experimental setup 35
- 5.4 Sample droplet creation and characterization. 36
  - 5.4.1 Droplet evaporation 36
  - 5.4.2 Generating small droplets 36

5.4.3 Characterizing droplet size. 37
5.5 Testing 38
5.6 Experimental findings. 38
5.6.1 Measurement results. 38
5.6.2 Measurement results interpretation 40

6 Conclusion & recommendations 43
6.1 Conclusion 43
6.2 Recommendations 46

Bibliography 47

1
Introduction

The semiconductor industry is rapidly growing as the demand for computing power in electronics continues to increase. In this race to get as many transistors on a single chip, boundaries are constantly being pushed. Feature sizes keep decreasing and processes keep speeding up, giving rise to a wide variety of new problems. In this multi-billion dollar industry, time is very valuable, so there is a high demand for optimizing every single process step.

Computer chips or integrated circuits (ICs) consist of complex structures that make up a vast network of transistors. At the core of manufacturing these ICs is a process called photolithography. Structures are formed out of several, typically 20 to 30 layers, each layer requiring a variety of physical and chemical process steps. These structures are very small; currently the most advanced ICs have feature sizes in the range of several nanometers. Effects like thermal expansion and nano- or microparticle contamination of the substrate can cause misalignment of layers or defects in the circuit. As a result, there are tight tolerances on the temperature and contamination levels of the silicon wafers.

1.1. Wafer conditioning at VDL-ETG

To bring the wafers within these tight tolerances, VDL-ETG implemented contamination control and thermal conditioning to the Atmospheric Wafer Handler (AWH). The current state of the art for thermal conditioning at VDL-ETG is their Thermal Stabilization Unit (TSU). The TSU consists of an aluminum block with cooling channels, that keep its temperature very close to the desired temperature. When the wafer must undergo the thermal conditioning, the TSU is brought up close to the back side of the wafer, and air is passed through this block - and over the wafer. When the wafer has reached the desired temperature, the TSU is moved away from the wafer. The time this system takes for thermal conditioning is roughly 10 seconds.

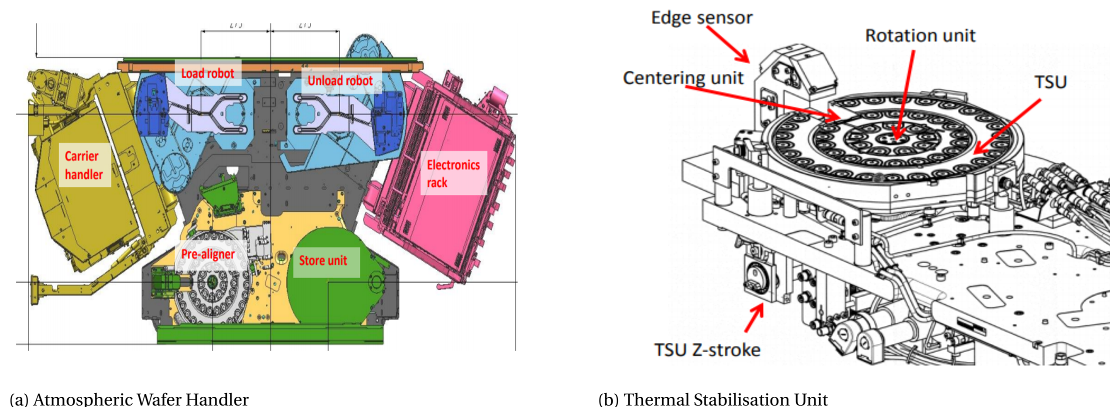

(a) Atmospheric Wafer Handler

(b) Thermal Stabilisation Unit

Figure 1.1: Overview of the state of the art at VDL-ETG

Proposed new design: Water bearing

Thermal conditioning is the bottleneck of the cycle time of the system. By shaving off thermal conditioning time, we can directly increase the throughput of the system, directly making it more valuable to the customer.

To improve this conditioning time a redesign was proposed. The design consists of two water bearings, placed directly under the rotating wafer. These water bearings circulate a thin layer of thermally conditioned demineralized water, which directly contacts back side of the wafer. The wafer will rotate over these water bearings until the desired thermal properties are met. Since the specific heat and thermal conductivity of water are much higher than that of air, this will drastically cut down the time required for conditioning.

However, this design also introduces new challenges. The conditioning process will leave a residue of water on the back side of the wafer. The wafer must be completely clean before it undergoes the lithography process, so this water must be removed.

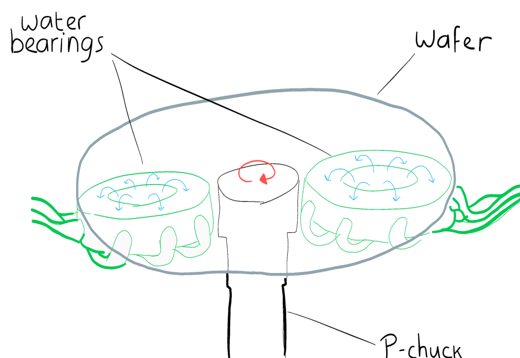

Figure 1.2: Schematic overview of water bearing setup

Dry unit and surface inspection tool

In an attempt to tackle these new challenges VDL-ETG proposed the design of a dry unit to remove this water residue, and a surface inspection tool to check if the surface is actually dry.

Since the end goal is achieving a reduction in thermal conditioning time, both the dry unit and the surface inspection tool must have strict requirements on thermal effects and cycle time. Since the dry unit has not yet been designed, its properties are not yet known. The available errors will be budgeted over these two designs.

1.2. Project goal

The goal of this project is designing and validating a surface inspection system that can rapidly detect micrometer water droplets on the back side of a silicon wafer. The exact requirements of this research goal will be discussed in the next chapter.

The full design study can be broken up into smaller steps, which have been set as project subgoals.

Firstly the system requirements, and nice-to-haves must be mapped out, along with the systems environmental conditions. Then a broad search must be done for viable concepts. Out of these concepts a justified selection must be made. A design based on first principles must be performed to create a system that works on paper. Subsequently a prototype must be realized and tested, that can show a proof of concept for the design, and possibly reveal flaws, or factors that have been overlooked. Then an iterative design process will be followed to reach a finalized design.

The subgoals for this design project are summarized in the following list.

- Setting up the system requirements and wishes
- Concept generation and selection
- Make a design based on first principles
- Build and test a prototype
- Finalize detailed design

2
Requirements

Requirements are the bounding factor of any design study, they set the playing field of the research. Our philosophy is that a meticulous requirement study is essential for a smooth design process. Changing course gets more time consuming the further you are in the design process, so it is crucial to spot potential dangers early on. The requirement study also reveals which parts of the design are critical. This allows us to better focus our attention on the parts that matter most.

The requirements are split up in must-have and nice-to-have requirements. Alongside these requirements this chapter also discusses the environmental conditions in which the system must operate.

2.1. Summary tables

The requirements and environmental conditions are summarized in tab. 2.1, 2.2 and 2.3. Section 2.2 elaborates on how the requirements and environmental conditions were acquired.

Must-haves

Property	Value	Remark
Measurement time	< 2 s	Priority, as low as possible
Detection range	>35 µm ⌀	
Droplet shapes	Round- , deformed droplets and finite films	
False negative rate	≤ 1 per 6200 wafers	
False positive rate	≤ 1 per 15 wafers	
Size measurement	Boolean	Only separate < and > 35 µm
Bulk dT	< 3 mK	} Details in fig. 2.4
Temperature non-uniformity	< 1 mK	
Build volume	Approximately 300 × 150 × 120 mm	Details in fig. 2.5a

Table 2.1: Must-have requirements of the study

Nice-to-haves

Property	Value	Remark
Build volume	Approximately 300 × 150 × 70 mm	Details in fig. 2.5b
Size measurement	Measure droplet diameter	
Droplet position accuracy	< 5 mm	
Final product cost	Low	

Table 2.2: Nice-to-have requirements of the study

Environmental conditions

Property	Value	Remark
Wafer rotation	$1.3 - 39\,\mathrm{rad\,s^{-1}}$	
Wafer warp	$< 450\,\mu\mathrm{m}$	Peak-to-peak, measured at the edge
Clean room class	ISO 3	
Ambient temperature	$22\,^{\circ}\mathrm{C}$	
Ambient pressure	1 atm	

Table 2.3: Environmental conditions of the study

2.2. Clarification

In this section we will discuss how the values shown in tab. 2.1, 2.2 and 2.3 were derived.

Measurement time

The goal of the new design is to reduce the conditioning time and thus increase the overall throughput of the machine. As you can see in fig. 2.1, the old TSU design had a conditioning time of 9.9 seconds and a cycle time of 17.0 seconds.[4] During this conditioning time the temperature of the wafer was brought into spec, during this process the centering and "rotation to notch" of the wafer also take place. However the last three seconds of conditioning do not overlap with other process steps. This means that if we can reduce the conditioning time by 3 seconds, we can directly decrease the cycle time of the machine by that amount. Reducing the conditioning time even further can be beneficial, but only if there is also some improvement in cycle time of the centering- and "rotation to notch" of the wafer. However beside the thermal conditioning, drying and inspection of the wafer must now also be performed within this thermal conditioning time. The inspection can be done (partly) simultaneously with the drying, but not simultaneously with thermal conditioning since the water will not yet be removed at this stage. Since the water bearing design is not yet finalized, the time required for the thermal conditioning with the new design is not yet known, so we make the assumption that the time required for the thermal conditioning will be roughly 5 seconds. To reach a reduction in cycle time of 3 seconds, we need a measurement time of less than 2 seconds. If the rest of the design allows it, we can reduce the measurement time even further - however it is not guaranteed that a further reduction in measurement time is beneficial for the throughput of the machine.

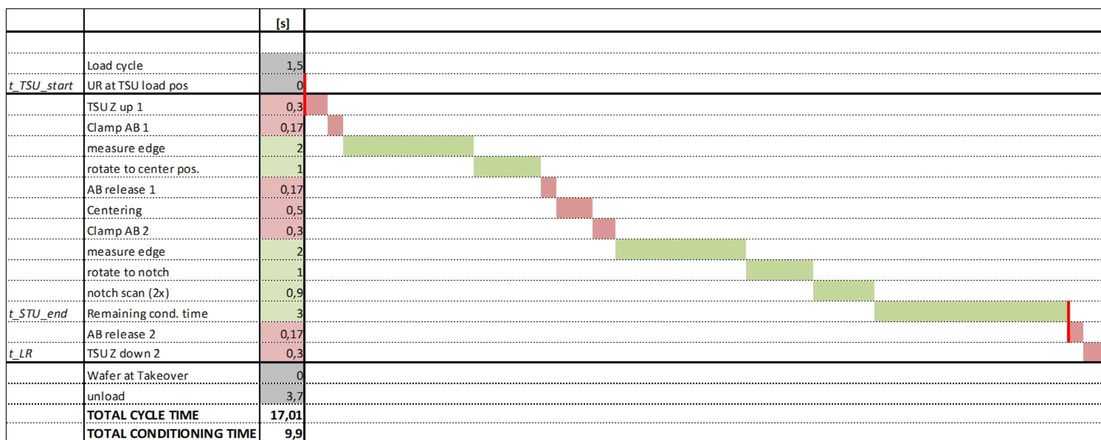

Figure 2.1: Overview of the timing of old TSU design[4]

Detection range

Demineralised water is being used by the water bearing design, meaning that evaporating droplets will not leave any mineral residue on the wafer that can cause problems for the photolithography process. This means our detection range is solely bound by the evaporation time of a droplet. Two formulas for droplet evaporation times are plotted in 2.2. These formulas assume a constant contact angle- and a constant contact radius

respectively.[18]. The real evaporation curve is somewhere between these extremes. If droplets evaporate completely before the wafer enters the vacuum chamber, the droplets can not have a detrimental effect on any other subsystem. When we take the worst case scenario, i.e. 130° following the constant angle evaporation curve, droplets with a diameter of 35μm would still evaporate completely in 4 seconds, which is the current unload time of the wafer after conditioning. It is unlikely that the surface of the wafer is this hydrophobic, and that the evaporating droplet behaves exactly as described. Since the hydrophobicity of the wafer is unknown due to different coatings that can be applied to the bottom side of a wafer, we simply assume the worst case scenario. By doing so we can guarantee that the design will work regardless of the varying circumstances

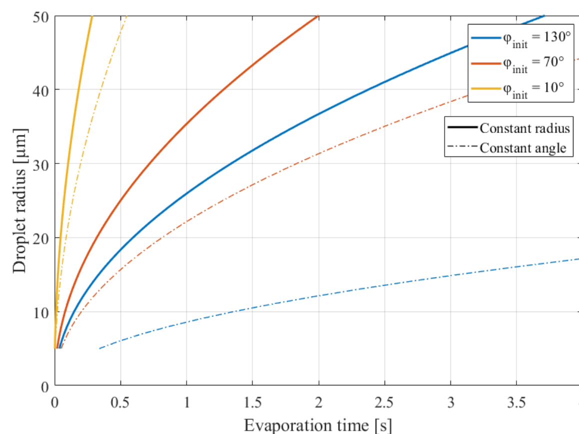

Figure 2.2: Evaporation time of a single droplet of water on a silicon wafer, with the constant diameter and constant contact angle modelling respectively

Error tolerance

Engineers at VDL-ETG made it clear that water was not allowed to remain on the wafer because it would cause issues in the vacuum chamber. However, nobody could give a clear specification for how much water was still allowable. Therefore we must make some assumptions to get values of this error tolerance we can work with. There are four possible outcomes when doing measurements:

	True	False
Positive	Correctly measuring the presence of a droplet	Measuring a droplet when there is none
Negative	Correctly measuring the absence of a droplet	Not measuring a droplet when there is one

Table 2.4: Confusion matrix definition

Ideally the system would only have true positive and true negative measurements. However this is never possible in practice. Having a very low error tolerance also means that the requirements of the system must be very strict. Accepting some error rate allows us to relax these requirements slightly. As can be seen in table 2.5 we must quantify the amount of false positive- and false negative measurements that we accept.

False negative measurements are a big problem. They cause water to remain on the wafer undetected, which can cause problems when the wafer enters a vacuum. We assume that one droplet larger than 35 μm is allowed to pass undetected each day the system is operating. With the new measurement time, we aim for a total cycle time of 15 seconds, which would translate to 240 wafers per hour. This would mean we allow one false negative measurement per 6200 wafers.

False positive measurements are less crucial. When the system detects a droplet while in reality there is none, the detection loop simply must run another cycle to find out the wafer was actually clean of droplets. We can express this false positive rate in terms of added time per wafer. If we assume that one measurement cycle takes 2 seconds, we can estimate that we will only allow an increase of measurement time per wafer of 0.1s. This would translate to one false positive measurement per 15 wafers.

Firstly we must quantify what makes a measurement positive or negative. Intuitively one would think it is as simple as choosing any measurement containing no droplets or droplets with a diameter smaller than 35μm to be a negative measurement, and any measurement containing a droplet with a diameter larger than

35µm to be positive. However as the droplet sizes approach this boundary, more and more precision and accuracy are needed to correctly separate the droplet sizes. Approaching the problem in this way would set unreasonably high performance requirements to the system, which means that we would be solving a problem that does not really exist. Realistically we do not care too much what happens very close to this boundary. For example leaving a droplet of 34.9µm, or a droplet of 35.1µm on the wafer would have effects further up in the system that are indistinguishable from each other. To prevent focusing on the wrong part of the design, this fact should be represented in the system requirements.

To account for this we have chosen to implement a transition region in which we ignore measurements when judging the error tolerance of the system. In this region we allow ambiguity between positive and negative measurements.

This confusion region is chosen to be between 25 and 45µm.

	Positive measurement	Confusion region	Negative measurement
Range	$D \leq 25$µm	25µm $< D <$ 45µm	$D \geq 45$µm
Error rate	$e \leq 1$ per 6200 wafers	-	$e \leq 1$ per 15 wafers

Table 2.5: Summary of error rate tolerances

Droplet shapes

Droplets on surfaces come in all shapes and sizes. Which shapes are possible depend on the droplet size, hydrophobocity of the surface. Highly hydrophyllic surfaces have a high surface energy relative to the surface tension of the water and vice versa for highly hydrophobic surfaces. This hydrophobicity determines the contact angle ϕ. The bottom side of wafers are coated in a wide variety of coatings, so we have to assume that the hydrophobicity of the surface is completely unknown. The smaller the droplets get the more they tend towards spherical caps, however the contact angle still remains unknown. Larger droplets can however take a wide variety of shapes, including water films. However since the water bearings do not cover the entire wafer surface, we can assume that the water film is finite, and thus has an edge somewhere on the wafer. This is important because many detection techniques cannot detect water films directly, but they can detect film edges.

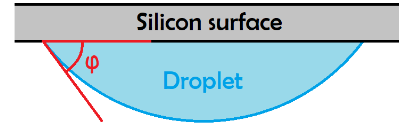

Figure 2.3: Contact angle of the droplet illustrated

Temperature requirements

The TSU had very strict thermal requirements. These requirements can be seen in tab. 2.6.

Average wafer temperature	$0\,\text{mK} < \Delta T_{av} < 25\,\text{mK}$
Average reference temperature	$\lvert\Delta T_{\text{av-ref}} - T_{LCW}\rvert < 25\,\text{mK}$
Temperature non-uniformity	$\Delta T_{\text{non-uni}} < 11\,\text{mK}$
Temperature gradient	$\text{dT}/\text{dR} < 100\,\text{mK}$
Thermal signature TSU	$\Delta T_{\text{non-uni ref}} < 2\,\text{mK}$ for length scales $< 100\,\text{mm}$

Table 2.6: Thermal requirements from TSU specifications sheet[4]

These requirements still need to be budgeted over the water bearings, dry unit and surface inspection system. Since these requirements are confusing at first sight, we decided to simplify the requirements to just an average wafer temperature-, and a temperature non-uniformity requirement. We estimated that only a small fraction of the total budget was needed for the surface inspection, so we settled on $\Delta T_{\text{bulk}} < 3\,\text{mK}$, and $\Delta T_{\text{non-uni}} < 1\,\text{mK}$ for the surface inspection. These requirements are specified in fig. 2.4

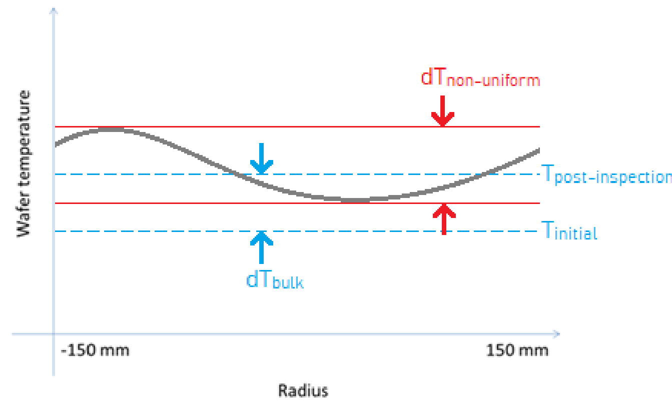

Figure 2.4: Definition of the temperature requirements. The grey curve is the temperature profile of an arbitrary wafer, and the blue dotted lines the average temperature of an arbitrary wafer before and after conditioning

Available volume
The available space in the AWH is approximately equal to the wafer surface, being extruded down by 12 cm. Since the water bearing setup is already in place, we have divided the remaining build volume over the dry unit and the surface inspection tool. This build volume can be seen in fig. 2.5a. For backwards compatibility it would be nice to fit the whole setup (water bearings, dry unit and surface inspection tool) in the build volume of the old TSU as can be seen in fig. 2.5b. However this would limit the height of our design to 70 mm. This backwards compatibility is therefore added in the nice-to-haves.

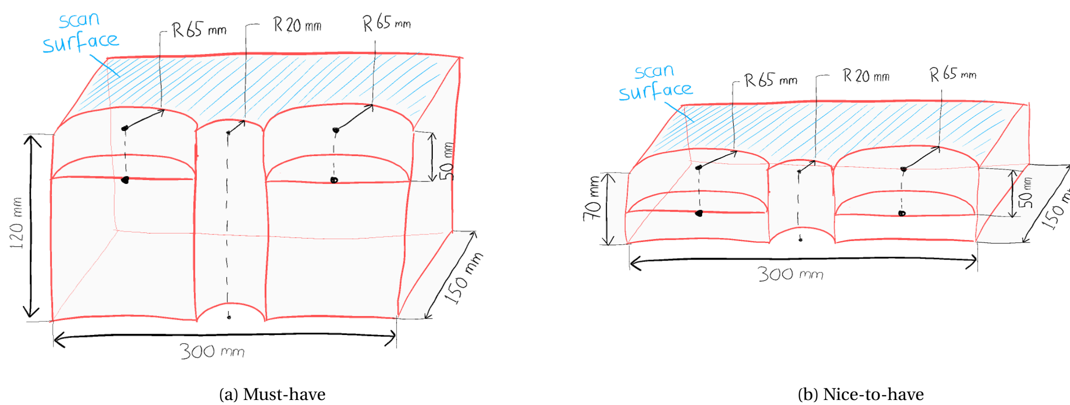

(a) Must-have

(b) Nice-to-have

Figure 2.5: Available volume

Droplet sizing
For the purposes of our system it is not needed to determine the dimensions of the droplets, the only question we need to answer is: Are there any droplets present with a diameter above 35µm. It could however be useful to use that information to characterize the water bearings or the dry unit. Another purpose could be to use the diameter information for an advanced risk calculation to tweak the trade-off between throughput and risk. Therefore droplet sizing has been put in the nice-to-haves list.

Budget
The budget of the project is not well defined. According to one of the AWH system architects conditioning is the temporal bottleneck of the AWH, thus decreasing conditioning time will directly increase throughput. However the design is also dependent on the success of the water bearings and dry unit subsystems. The budget will be done in consultation with the company during the project. However low cost is obviously al-

ways a good thing when making a design, thus it has be incorporated in the nice-to-haves list.

Droplet location accuracy
Since the dry unit is being designed as a static system, which does not use feedback information from the measurement, it is not needed to determine the droplet locations. However it could potentially be useful in the case that the dry unit will use feedback control in a future design iteration. Another reason why it would be potentially useful, is again for the characterisation of the water bearing and dry unit. The dry unit will use a thin air knife to remove excess water from the bottom side of the wafer. Typically the exit nozzle is a slit of around 1 mm thick, if we want to use the droplet location information for water removal this is also the order of magnitude of location accuracy we will need.

Wafer rotation
The wafer rotation speed is a parameter we can still choose freely. However there is a maximum acceleration that can be put on the wafer of $39\,\mathrm{rad/s^2}$. Since we need to beat the current cycle time of 17.0 seconds, we chose to limit the rotation speed to the speed after 1 s of spin up. For the purposes of droplet detection it makes sense to choose this speed such that a wafer can be measured in a single revolution. So it will likely be around one revolution per 2 seconds or $3.1\,\mathrm{rad\,s^{-1}}$

Wafer warp
The wafer has some warp and wobble when rotating on the vacuum P-chuck. Together these contributions add up to $450\,\mu\mathrm{m}$ peak-to-peak, perpendicular to the wafer surface at the edge of the wafer. In the test setup these contributions will be higher however.

3
Concept generation and selection

The concept is the foundation of your design. Basing your design on a bad concept can cause a lot of problems later on in the design process. And changing concepts very late in the design means that you have done a lot of work for nothing. It is important to execute this step of the design process meticulously.

For the concept generation we first start with a wide scope to make sure you do not miss any crucial solutions. Then we will try to judge these concepts and narrow down the scope to one or two concepts for the first principles design.

3.1. Detection principles

In order to start with this wide scope we go back to the most basic way to look at this problem: What methods are there to detect these water droplets?

Bright field imaging

Conventional optical imaging, or bright-field imaging, is the most straightforward way of imaging the wafer surface. This method works by illuminating the object with a light source, and then directly measuring the reflected light with photodetectors. Each pixel in the image plane maps to a point in the real space, and the pixel intensity relates to the irradiance of light received from that point in space. The mapping is usually done by a system of lenses and mirrors, that refract and reflect the light in such a way that a scaled version of the object is projected onto a photodiode array like a CCD or CMOS sensor, but can also be done through . For droplet detection this means that your measured signal will be a mix of the information you're interested in, and a background signal. There are ways of reducing this background signal, for example by choosing a smart focal range. But there will always need to be some signal processing to extract the useful information from your image.

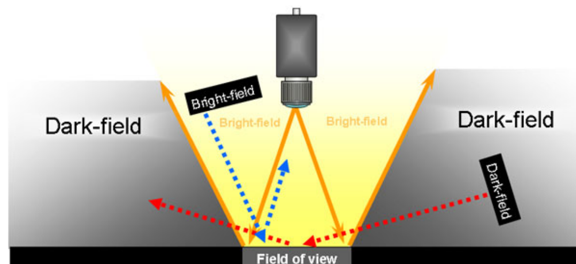

Figure 3.1: The difference between dark-field and bright-field illumination [1]

Dark field imaging

Dark-field imaging is very similar to bright field imaging. However instead of measuring the direct illumination, the optical system is designed in such a way that the direct illumination that reaches the photodetector is minimized. This means that the photodetector will see a much larger disparity in irradiance between sample and background. This results in a much larger contrast than can be achieved with bright field imaging.

For inspection of non-transparent surfaces, dark field imaging proves to be especially useful if the surface is mirror-like. When diffuse reflections are minimized, the system is able to detect very small anomalies in the otherwise smooth surface. The irradiance at the detector is usually quite low for dark-field imaging. Photodetectors can easily pick up this small signal, however, if other light sources can also reach the photodetector they can easily blow out the signal.

Dark-field imaging is commonly used in microscopy[8] and in surface inspection[19]. Since it is commonly used for flaw detection of highly reflective surfaces it seems to be very suitable for this project.

Absorption imaging

In bright field and dark field imaging, we use the fact that light reflects and refracts due to the difference in refractive indices of the water and air, and measure the change in optical path that results from it. However, there are many other properties of light we can use for detection. Light is not only refracted and reflected by water, it also attenuates due to absorption. The absorption of visible light in water is very low, however wavelengths outside the visible spectrum get much more strongly absorbed by water, as can be seen in fig. 3.2a. The attenuation due to the strong absorption in water can be used to detect small water droplets. In literature absorption imaging is being used for tomography[20], layer analysis of graphene[11] and for characterization of ultracold atoms[16]. No resources were found for absorption based imaging techniques for detecting water, or surface inspection applications, so the feasibility of this method remains uncertain.

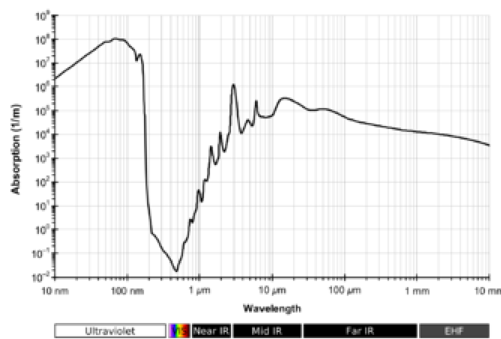

(a) Absorption: Absorption spectrum of light in water[3]

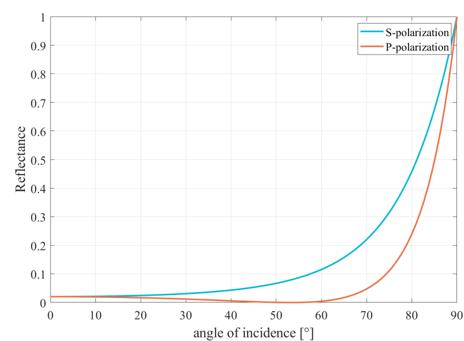

(b) Polarization: Reflectance of s- and p-polarized of water under varying incident angles [2]

Figure 3.2: Additional useful properties of light

Polarization imaging

Another property we can use for detection is the polarization state of the light. The reflectivity and transmittance of a water surface is dependent on the polarization state of the incident light. This means that when unpolarized light is incident on an air-water boundary, the polarization states of the reflected- and transmitted light will be different. The reflectances follow the following formula, which are plotted in fig. 3.2b. Polarization imaging is being used for the detection of skin diseases [14] and for the macroscopic reconstruction of specular surfaces [15]. Polarization has also been used for the detection of surface-deposited dielectric nanoparticles[17], however with the detection speed in the order of magntiude of a few $\text{cm}\,\text{s}^{-1}$ this method is too slow for our purposes.

The reflectance of s- and p-polarized light follow the formulas:

$$r_{\perp} = \frac{n_i \cos\theta_i - n_t \cos\theta_t}{n_i \cos\theta_i + n_t \cos\theta_t} \quad (3.1)$$

$$r_{\parallel} = \frac{n_t \cos\theta_i - n_i \cos\theta_t}{n_i \cos\theta_t + n_t \cos\theta_i} \quad (3.2)$$

Interferometry

Interferometry is a technique for measuring very small displacements. There are a wide variety of interferometers, but they are all based on the same principle. A coherent source is split up in two paths, and recombined before hitting the detector. The two beams have interference with each other, creating fringe patterns that result from a difference in path length. Interferometry can measure very small displacements, and is commonly being used for surface metrology, measuring displacements of precision stages and surface roughness analysis[6]. Using interferometry for measurements of 25μm and above, seems very inefficient, since these dimensions are much larger than the wavelength of light.

Acoustic imaging
Acoustic imaging makes use of ultrasonic transducers that can convert electrical energy to sound waves and vice versa. High frequency sound waves are generated, that bounce off the target, and back to the transducer. With the two-way trip time, and the speed of sound in air, you can calculate the distance the sound traveled. Some applications of acoustic imaging are medical ultrasound tomography, ultrasonic distance sensors, and sonar imaging systems. The resolution of these techniques is however insufficient.[7, 9],

Since we are interested in very small features, acoustic imaging does not seem to be the best solution for the problem. Not only are the distances that you want to measure very small (the height of the droplet). The surface area of the droplet is also very small. Since it is very difficult to focus light to a small spot, your relevant signal (reflection off the droplet) will be very low in amplitude compared to the background signal (reflection off the wafer). This means it will be very difficult to pick the measurement out of the noise.

Other methods
There are more methods available, like measuring the mass change or the change in electrical resistivity of the wafer in the presence of water droplets. However these methods proved to be unfeasible with a simple back of the envelope calculation, and will not be thoroughly discussed here.

3.2. Light scattering

Most viable detection principles rely on a changing light path due to interaction with the droplet. Therefore we have chosen to first look at the characterization of this light-droplet interaction. Due to refraction, reflection and diffraction, small particles redirect light in every direction. The in a process called scattering. The scattering particle acts as a point source of light in the far field, however the intensity can be different in different directions.

Angular scattering pattern distribution and intensity dependent on[12]:

- Size of the particle w.r.t. wavelength of light
- Polarization state of light
- Shape of the particle
- Index of refraction of the particle w.r.t. surrounding medium

Light scattering by particles can be divided into three regimes: (a)The Rayleigh regime, for particles much smaller than the wavelength of incident light, (b)The Mie regime, for particles with sizes similar to the wavelength of incident light, and (c)the geometric regime, for particles much larger than the wavelength of incident light. In general for all cases the total amount I_s, the total amount that a particle scatters for a given intensity of illumination follows the proportionality[12]:

$$I_s \propto \lambda^2 f(\alpha) \qquad \text{with} \quad \alpha = \frac{\pi d}{\lambda} \tag{3.3}$$

$$\begin{array}{lll} \text{for Rayleigh scattering:} & f(\alpha) = \alpha^6 & \\ \text{for Mie scattering:} & f(\alpha) = \alpha^n & \text{with } 2 < n < 6 \\ \text{for geometric scattering:} & f(\alpha) = \alpha^2 & \end{array}$$

In the large particle case the angular scatting pattern has two major contributors[12]:

- Roughly half of the scattered light is caused by diffraction, this creates a very narrow forward beam within an angle $\theta_d = \frac{25}{d}$ where d is the particle diameter in µm
- The reflected and refracted portion whose angular distribution depends on the reflectivity of these large particles

For this research we're interested in a scattering particle deposited on a flat surface however. In that case we can identify the following components of reflected/scattered light from this particle-surface superposition, assuming the beam cross-section is larger than the particle diameter[12]:

- Direct specular reflection from the surface
- Diffuse reflection from the surface (due to distributed imperfections)
- Direct scatter from the deposited particle (limited to 2πsr)
- Surface-reflected particle scatter (from the other 2πsr of the particle scatter)

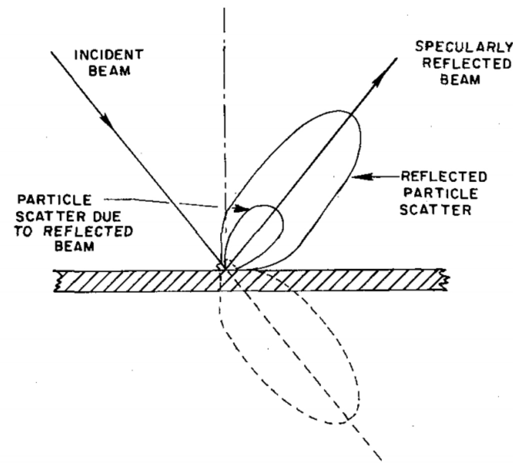

Figure 3.3: Scattering pattern from a surface deposited particle[12]

The scattering and reflection components mentioned above interact with each other through interference. Any deviations in particle shape will further complicate the angular scattering pattern. The various scattering and reflection components interact with each other through wave interference, and any particle shape irregularities will complicate the resultant angular scattering pattern even further. With the complicated nature of light scattering, it is very hard to accurately reconstruct droplet sizes just from measuring the intensity of scattered light.

We can solve this issue by choosing a smart design however. Firstly we identify the factors that influence this angular scattering profile, and what part of this profile our detectors will observe. These factors are the following:

- Angle between incident beam and wafer surface
- Angle between (reflected) forward scattering direction and detector
- Numeric aperture (NA) from the point of scattering to the detector
- Intensity of the incident light
- Size of the droplet

Some factors that influence the angular scattering profile have not been included in this list on purpose. The wavelength and polarization state of the light, and the index of refraction of the particle w.r.t. surrounding medium have not been included because they will stay constant. And the shape of the droplets has not been included because the design will have no influence on droplet shapes.

By choosing a design such that these factors stay as constant as possible, we can eliminate a lot of unwanted signal variations caused by changes in the scattering profile, and changes in which part of the profile reaches the detector. It is still very difficult to predict the droplet size with only the quantity of light energy reaching the detector. However, we have created a system that is very robust. A droplet of a certain size will always give nearly the same signal strength, regardless of where on the wafer or when in time it is being detected. This means that you can simply calibrate the system by placing a droplet of known size.

We can even further improve the robustness if we can make the design in such a way that we measure the frontal lobe of the scattering profile. This section of the scattering profile is the least sensitive to slight changes of the system.

3.3. Performance criteria

In order to judge the strength of a concept, we must first set up the performance criteria. These criteria will reflect how well a design is expected to perform. The performance criteria that have been set up are the following:

- High discriminative power

- High measurement speed, including image processing
- No significant impact on wafer temperature

3.3.1. Discriminative power

One of the most important metrics in our design is the discriminative power of the system. In other words, the ability to separate positive (the presence of a droplet, greater than the threshold) from negative measurements.

This includes factors like how high the signal-to-noise ratio is, how prone it is to errors, how well it can distinguish droplets from the particles or surface damage that can be expected on the back side of the wafer, and if it can also detect for example a water film on the wafer. But most importantly, how well it can relate a signal to a droplet size.

As mentioned in section 3.2, to reliably relate a signal to a droplet size, a system must use the frontal lobe of the scattering profile, and keep the following factors constant:

- Angle between incident beam and inspection surface
- Angle between (reflected) forward scattering direction and detector
- NA from inspection area to detector
- Intensity of illumination

3.3.2. Measurement speed

The measurement time is another important performance criterium. The measurement time is dependent on a lot of different design choices. However in the concept phase we can simply make an estimate of the measurement speed, and distinguish between methods that rely heavily on image processing and methods that directly give useful data. Since we are measuring in situ the processing time will simply add up to the measurement time.

3.3.3. Effect on wafer temperature

The surface inspection tool is not allowed to have a large effect on the temperature profile of the silicon wafer. The factors of the temperature profile that are important are:

- Effect on the average wafer temperature
- Effect on the temperature non-uniformity

Average wafer temperature

The average wafer temperature is affected by the illumination source of the measurement system. The main driving factors that influence the wafer temperature are the power of the illumination source and the exposure duty cycle.

There are also other sources of heat generation, like joule heating of electronic components, or heating due to friction of moving components. However we have chosen to ignore these contributions for now.

To give an idea of the magnitude of this effect, some back of the envelope calculations were performed, choosing some arbitrary values for source power and exposure time. These calculations show that when illuminating the wafer for 5 seconds with a 5 mW light source, the average temperature of the wafer increases by approximately 1 mK This is well within spec. If we are to increase the power of the illumination source much above 5 mK we should take the bulk temperature into account, otherwise we can just ignore this.

Temperature non-uniformity

The temperature non uniformity is also affected by the illumination source of the measurement system. The uniformity of illumination together with the thermal conductivity of the material determine the temperature profile after measurement. To keep the temperature non-uniformity as low as possible we must simply keep the illumination profile as uniform as possible.

3.4. Concepts

Combining the information about detection principles, light scattering, and performance criteria we can now generate concepts.

3.4.1. Concept 1: Dark-field camera inspection

This concept uses the most obvious visual inspection system: a light source and a camera. A light source illuminates the wafer surface under a grazing angle. The camera is placed with its central axis perpendicular to the wafer surface. This dark-field configuration makes the entire image black - except for when droplets interact with the light, and redirect it towards the camera. The static camera takes snapshots of sections of the illuminated wafer as it is rotating underneath - until the entire wafer surface is mapped. A sketch of this concept can be seen in fig. 3.4a. Directly linking a pixel intensity to a droplet size will be complicated, since the camera sees different sections of the scattering profile depending on the droplet location on the wafer. This means that image processing must be used to find the droplet sizes. The Nyquist-Shannon sampling theorem tells us that in order to reliably reproduce a droplet size, we require a pixel size that is smaller than half that droplet size. That means that in order to reconstruct droplet sizes of 35 µm we need pixels of 17.5 µm. The area of the inspection surface is roughly 0.07 m^2, which means that a pixel count of roughly 2.3×10^8 is expected for each wafer. To prevent motion blur of more than one pixel, an exposure time of less than 37 µs is required. This means that a very bright source is required to achieve the desired contrast. To reduce the thermal energy added to the wafer the source can be flashed briefly during exposure.

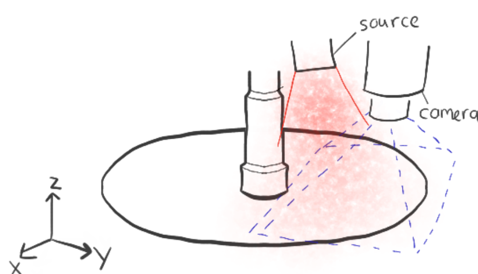

(a) Concept 1: Dark-field camera inspection system

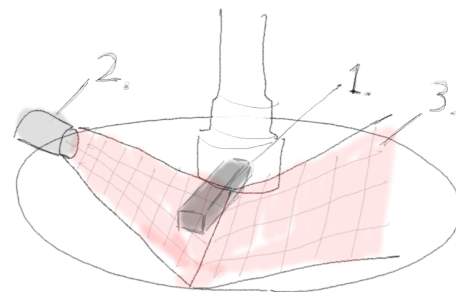

(b) Concept 2: Laser sheet scanner with diode-array, with 1) diode array/line scan camera, 2) source, 3) laser sheet

Figure 3.4: Concept 1 and 2 sketches

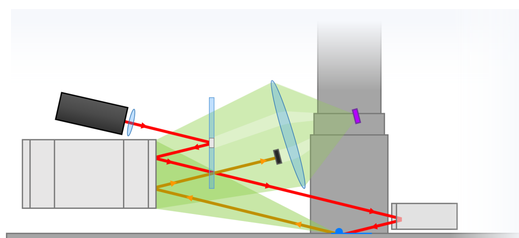

(a) Side view of concept 3: Synchronous dark-field flying spot scanner

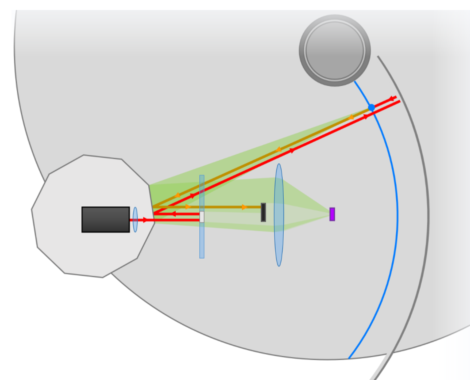

(b) Top view of concept 3: Synchronous dark-field flying spot scanner

Figure 3.5: Concept 3 sketches

3.4.2. Concept 2: Dark-field laser sheet scanner

This concept uses a laser sheet that creates a line of illumination in the radial direction of the wafer. The laser sheet grazes the inspection surface under a low angle and directly above the inspection line, a diode array or a line scan camera is placed to measure the signal. The advantage of this concept is that the sensors can be relatively close to the inspection area, allowing for a large NA to be achieved. However in this layout the measurement is taking place perpendicular to the frontal lobe of the scattering profile - where the scattering intensity is lowest. Additionally, since the laser sheet is basically a stretched Gaussian beam, there will be a large variation in illumination intensity across the inspection line. Warp of the wafer will cause errors, shifting the illuminated line in the tangential direction of the wafer - which must be accounted for. An illustration of the concept can be seen in fig. 3.4b.

3.4.3. Concept 3: Synchronous dark-field flying-spot scanner

In this concept the illumination is done with a laser beam that is focused to a spot, which is deflected by a some form of deflection optics. The spot moves over the wafer surface in a line, while the wafer rotates underneath tangential to the direction of the scan line. These two tangential motions make it possible to scan the whole wafer surface. By shining the laser on the polygon under an angle w.r.t. the plane of rotation of the polygon, the deflected beam follows a conical section. This results in a heavily bowed scan line - but with a constant distance to each point on the scan line. By placing a cylindrical mirror behind the scan line, perpendicular to the wafer surface, the laser beam is reflected back to the polygon. Because the returning beam is parallel to the outgoing beam, reflection on the polygon effectively reverses the scanning motion. This makes the returning beam stationary after reflection. A small circular obstruction blocks the direct returning beam, before a lens focuses all the light that passes this obstruction on a detector. The geometry of this concept yields a constant illumination, angle of incidence and angle of inspection, and NA for each point on the wafer - which is very useful for directly linking a signal to a droplet size. However the many reflections make this design very prone to angular errors. An illustration of the concept can be seen in fig. 3.5.

3.5. Concept selection

The dark-field camera inspection concept is the simplest to realize. However the concept requires image processing to function. The images contain roughly 280 million pixels, and must be processed in a fraction of a second. Possibly there are smart algorithms available that can make this work, but as a mechanical engineer it is difficult to predict whether this is feasible and what the effect would be on the error rates. The laser sheet scanner can work without image processing, however the illumination does vary over the scan line, which must be compensated for. Additionally the wafer warp can cause scan line errors which can further decrease the performance of this concept. The detector measures almost perpendicular to the frontal lobe of the scattering profile, where the scattering intensity is lowest, however the NA that can be achieved is quite large. Finally the synchronous dark-field flying spot scanner concept solves these issues elegantly: Image processing is not required for this concept to function since the intensity of the illumination, incident angle, view angle and NA are all independent of location on the scan line. The fact that this concept measures in the frontal lobe of the scattering profile - while rejecting the direct beam, gives an excellent signal strength. However the high component count makes this the most complicated design to realize, and the large number of reflections makes this design prone to angular errors. The dark-field flying spot scanners excellent signal power and insensitivity to droplet location are so core to the design problem that this concept has been selected for this design problem - regardless of its inherent sensitivity to angular errors and its complicated design.

	discriminative power	measurement time	wafer heating
Concept 1: Dark-field camera inspection	+	+-	+-
Concept 2: Dark-field laser sheet scanner	+-	++	+-
Concept 3: Synchronous dark-field flying spot scanner	++	+	+-

Table 3.1: Summary of the concept selection

4
First principles design

Now that we have identified the synchronous dark-field flying spot scanner as the most promising concept, we can dive deeper into the design process. This chapter will discuss how the first principles were used to find a design that meets the performance criteria.

4.1. Design goals

We start our design process with the goal in mind. Knowing which system parameters directly influence the performance will help guide us through the design process. In earlier chapters we have determined that the largest driving factor for system performance is the discriminative power. We know what that means discriptively, but now we must quantify this concept.

4.1.1. Quantifying discriminative power

We must choose our design in such a way, that we can link the electrical signal we measure at the detector to a droplet size. This must be done to such a tolerance that only one droplet larger than 45 µm is allowed to bypass our system in every 6200 wafers. Additionally, once in every 15 wafers, a (false) positive measurement is allowed for droplet sizes below 25 µm, including no droplet at all. The concept of a synchronous dark-field flying spot scanner is mainly chosen because of the relative constant relation between droplet size and measured signal. This means we can directly relate a signal to a droplet size, with relatively low uncertainty, without the need for any complicated- and time consuming signal processing. There are four factors that determine how low this uncertainty is. Namely; 1) the signal strength, 2) the signal variation and 3) the noise.

Signal strength

The signal strength is simply the amount of current generated by the detector, as a result of the light scattered by a droplet. More specifically, it is chosen to be the average amount of current generated by a droplet of the threshold diameter. The threshold diameter is a diameter close to 35 µm, the exact definition of which is explained later in this section.

Signal variation

The dark-field signal variation (R_{DF}) is the amount of non-stochastic, non-repeatable variation (i.e. not noise) that our signal can experience for a constant droplet size. It is given as a percentage of the signal strength. Signal variation is driven by changes in illumination, changes in scattering profile and changes in FOV to the detector. Some of these sources of variation are repeatable and can be corrected for, such as the variation in FOV due to position on scan line. The non-repeatable contributions of signal variation (e.g. due to droplet location in spot, or defocus effects) are added to form the dark-field signal variation.

Signal noise

The signal noise is the amount of stochastic variation in the signal. There are three major contributions to noise in a photodiode; thermal noise, shot noise and dark current noise. Thermal noise (σ_{th}), also known as Johnson noise, is temperature dependent white noise generated by the load resistor. A higher temperature also means more thermal noise. Shot noise (σ_{sh}) is white noise that arises from the discrete nature of photons

and electrons. Shot noise scales with the average number of events per measurement. This means shot noise only becomes significant at low currents or low light levels. Dark current noise (σ_{dk}) is white noise caused by the constant current that exists even when no light is incident on the photodiode.[10] Because the noise is uncorrelated and of constant power spectral density, we can find the effective noise finding the root mean square of the noise sources.

$$\sigma_{eff} = \sqrt{\sigma_{th}^2 + \sigma_{sh}^2 + \sigma_{dk}^2} \tag{4.1}$$

Every time the system performs a measurement, these three factors yield a signal current. A threshold current (I_{thres}) is set up, so that signals above and below this threshold are seen as positive and negative, respectively. This threshold current is the average current generated by a droplet of the threshold diameter, which is a diameter close to 35 µm, chosen such that the noise power required for breaking the type 1 error rate is equal to the noise power required for breaking the type 2 error rate. In our requirements study we have set up a confusion region between 25 and 45 µm. Droplets in this confusion region are still measured, and labeled positive or negative according to the threshold current. However, they are not counted towards the false positive and false negative rate to judge system performance.

In order for a false measurement to occur, the combination of signal variation and signal noise must be so large that the measured droplet size ends up on the wrong side of the threshold diameter. Fig. 4.1 illustrates an example of a true positive measurement. If the noise and signal variation would be slightly larger, the measured droplet size would cross the threshold diameter, and thus yield a false negative measurement.

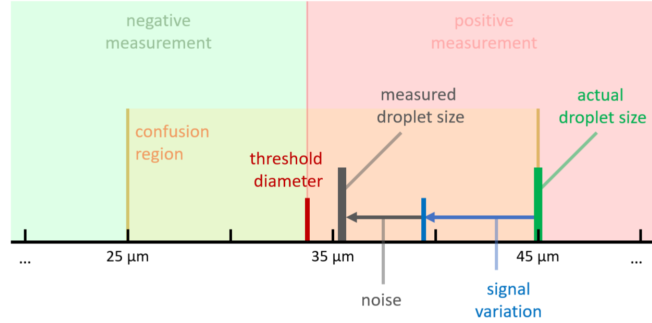

Figure 4.1: An example of a true positive measurement. The signal variation and noise cause the measured size to differ from the real droplet size. As long as this measured droplet size does not cross the threshold diameter the measurement remains true.

Completely modeling the signal variation is quite complex. To still guarantee the required system performance, we have chosen to simplify the design by always assuming the worst case signal variation (R_{DF}) instead. This way we make sure we are on the safe side - during the detailed design phase this extra room for error can be reduced to improve the design further.

We then know how large the noise contribution (X_{fn} and X_{fp} for false negative- and false positive measurements respectively) must be for a false measurement to occur. Because the effective noise is of constant power spectral density, we can use the cumulative distribution function (CDF) of the standard normal distribution to calculate the allowable noise power. The integral of the CDF of the standard normal distribution cannot be expressed in terms of elementary functions, so a numerical approximation must be used. This step is performed numerically in Excel. It is however important to note that we will be working with very large z-values. It is unclear if the Gaussian distribution is still a meaningful way to describe the noise behavior in the extreme tails of the distribution. However, it gives some grip on the problem, it's since in reality these extreme events never seem to happen rather than more than you expect - we expect to be on the safe side with this assumption.

$$X_{fn} = I_{thres} - I_{35}(1 + R_{DF}) \tag{4.2}$$

$$X_{fp} = I_{25}(1 + R_{DF}) - I_{thres} \tag{4.3}$$

$$P(x > X_{fn}) \quad < \quad \frac{1}{5760\ n_{pix}} \tag{4.4}$$

$$P(x > X_{fp}) \quad < \quad \frac{1}{20\ n_{pix}} \tag{4.5}$$

We must determine the systems dark-field signal strength, dark-field signal variation, and signal noise to show how well the system performs.

4.1.2. Quantifying wafer heating

Another important design goal is the effect on wafer temperature. As shown in sec. 2.2, the measurement must not alter the average wafer temperature by more than 3 mK. Additionally, the measurement must not induce temperature non-uniformities larger than 1 mK on a length scale of 100 mm.

The only factor of this design that influences the wafer temperature is the amount of laser light that is absorbed by the wafer. Metals that reflect electromagnetic radiation inherently absorb a fraction of the radiant energy. The fraction that is reflected is the reflectivity (R_{Si}). This material property is a function of wavelength(λ), angle of incidence(θ) and polarization state of the incident light. A database using the values from [5] is used to look up the correct reflectivity values.

In the design the direct laser beam reflects off the silicon wafer once. Assuming an unpolarized source, with power (P_{source}) and measurement time (t), the amount of radiant energy absorbed by the wafer during measurement is then:

$$Q \quad = \quad P_{source}\ t\ (\ 1 - R_{Si}(\lambda,\theta)\ ) \tag{4.6}$$

With the known wafer mass (m) and silicon specific heat (c_p), the absorbed radiant energy then translates to a change in average wafer temperature of:

$$dT_{bulk} \quad = \quad \frac{Q}{m\ c_p} \quad < \quad 3\ \text{mK} \tag{4.7}$$

The system scans the wafer in lines pointing radially outwards from the center. This non-homogenous lighting will cause some inherent non-uniformities in the wafer temperature. Slowly these non-uniformities will fade through thermal diffusion. The thermal diffusivity(α) is a measure of how fast this occurs. An estimation is made using the characteristic time(τ) to see which non-uniformities are relevant. Although conduction problems only asymptotically reach steady state, thermal conduction can be assumed to be at equilibrium when the time(t) is much larger than the characteristic time[**?**]

$$\tau \quad = \quad \frac{x^2}{\alpha} \tag{4.8}$$

In the axial direction (perpendicular to wafer surface), the relevant length scale(x) is the thickness of the wafer, 775 µm. With a thermal diffusivity of silicon of 88 mm^2/s, we find a characteristic time of 7 ms. In the tangential direction, the relevant length scale is the separation of the scanlines. This will be in the same order of magnitude, probably even lower. Because this characteristic time is much lower than the timescale of our measurement, temperature non-uniformities in both the axial- and tangential direction can be neglected.

In the radial direction, the relevant length scale is the length of a scan line, which is roughly 130 mm. For the radial direction this gives a characteristic time of roughly 192 s. Because the characteristic time of diffusion in the radial direction is much larger than the time scale of our measurement, we cannot ignore the temperature non-uniformity in this direction. The scan lines are drawn as curved lines from the edge of the chuck, near the center of the wafer, radially outwards to the edge of the wafer. In tangential direction the scan lines are evenly spaced. The amount of radiant energy absorbed by the wafer is directly proportional to the density of the scan lines at a certain position.

$$\frac{dT_{center}}{dT_{edge}} = \frac{\rho_{center}}{\rho_{edge}} = \frac{\left(\frac{N}{2\pi r_{center}}\right)}{\left(\frac{N}{2\pi r_{edge}}\right)} = \frac{r_{edge}}{r_{center}} = \frac{8}{1} \tag{4.9}$$

The temperature non-uniformity caused by the laser heating is not allowed to be larger than 1 mK. We can use eq. 4.9 to see that this will occur when $dT_{center} = 1.14\,\text{mK}$ and $dT_{edge} = 0.14\,\text{mK}$. Numerical methods have been used to determine this will occur when the bulk temperature changes by $dT_{bulk} = 0.74\,\text{mK}$. Since this value is reached before the bulk temperature limit of 3 mK is reached, the temperature non-uniformity ends up being the limiting factor for our design.

Combining the formulas from this section, we can say that:

$$dT_{bulk} = \frac{P_{source}\, t\,(1 - R(\lambda,\theta))}{m\, c_p} < 0.74\,\text{mK} \tag{4.10}$$

In order to know if the system meets the laser heating requirements, we must know the measurement time, laser power, laser wavelength and angle of incidence of light. Since the wavelength and angle of incidence only very slightly alter the reflectivity, we can say that the main driving factors are the laser power and measurement time.

4.1.3. Quantifying measurement time

After covering the discriminative power, and effect on wafer temperature, only one performance criterium is left; the measurement time. We simply choose a measurement time for our design, and calculate what performance we can achieve for that given measurement time. As discussed in sec. 2.2, reducing the measurement time further below 2 seconds does not guarantee an improvement in throughput. With more available time the it is easier to perform the measurement to the required specifications. Therefore we have chosen to set the measurement time at 2 seconds.

4.2. Gaussian beam propagation

To quantify the signal strength - and signal variation, it is important that we have a good understanding of how laser beams propagate through space. Ideal laser beams are assumed to be Gaussian. This means that the irradiance profile follows a Gaussian distribution w.r.t. the radial distance from the optical axis, at any point along its propagation. For peak irradiance I_0, beam radius w, and propagation distance z, the radial intensity profile is given by the following function:[13]:

$$I(r) = I_0\, exp\left(\frac{-2r^2}{w(z)^2}\right) \tag{4.11}$$

Since a Gaussian distribution theoretically has an infinite width, it is not easy to define the diameter of the beam. The convention of the $1/e^2$-diameter is mostly used. As illustrated in fig. 4.2, the $1/e^2$-diameter is defined to be diameter at which the irradiance is equal to $1/e^2$ (approximately 13.5%) of the peak irradiance. Whenever a beam diameter- or spot size is mentioned in this thesis, the $1/e^2$-diameter is what is being referred to.

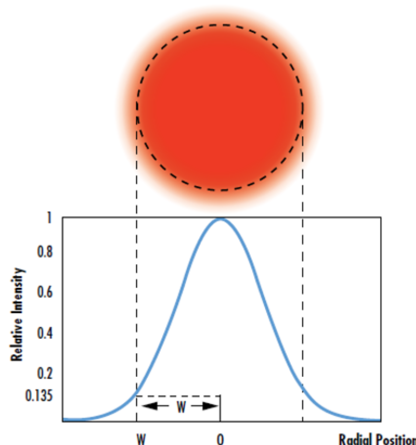

Figure 4.2: An illustration of a Gaussian beam profile and the $1/e^2$ beam diameter[?]

In ray optics we assume that an ideal lens focuses a collimated beam to an infinitesimally small spot. This is however not realistic. Due to diffraction effects there is a limit to how small a laser spot can be. This is

illustrated in fig. 4.3. The smallest waist of a focused laser beam is referred to as the minimum beam waist ($2w_0$). This diameter follows directly from the wavelength (λ) and divergence (θ) of the laser beam. When focusing a collimated laser beam, the divergence can be expressed as a beam diameter at the lens (D) and lens focal length (f).

$$2w_0 = \frac{2\lambda}{\pi\theta} = \frac{4\lambda f}{\pi\theta D} \tag{4.12}$$

Near the minimum beam waist the wavefront is flat, and the beam diameter stays relatively constant. A metric that quantifies how large this region is, is the Rayleigh length (z_r), or Rayleigh range. The Rayleigh length is defined as the propagation distance from the best focal point to the point where the beam waist reaches $w(z) = \sqrt{2} \times w_0$. This means that at the Rayleigh length, the cross-section of the beam is twice as large as the best focal point cross-section, and the irradiance half of the irradiance at the best focal point.

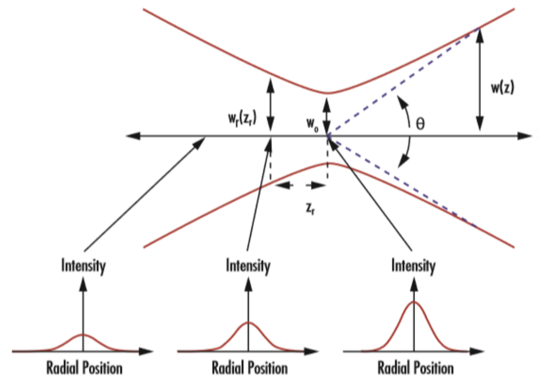

Figure 4.3: An illustration of diffraction effects limiting the minimum beam waist (w_0) - and the definition of the Rayleigh range (z_r).[**?**]

The Depth of Field (DOF) is the propgation distance during which the beam waist remains under this Rayleigh value. Since the Rayleigh range works on both sides of the minimum beam waist, the DOF is simply twice the Rayleigh length.

$$DOF = 2z_r = \frac{2\pi w_0^2}{\lambda} \tag{4.13}$$

The equation that describes the beam radius as a function of the propagation distance is then:

$$w(z) = w_0\sqrt{1 + \frac{(z - z_0)^2}{z_R^2}} \tag{4.14}$$

4.3. Scanning geometry

The layout and geometry of the scanner play an important role in finding the signal strength and signal variation. This section will detail the geometry of the big role in finding the signal strength and signal variation.

4.3.1. Scan lines, polygon duty cycle, scan angle and radial scan distance

Due to the nature of reflection, rotating the polygon by an angle, will induce twice that angle on the reflected beam. The laser beam is incident on the polygon under an angle w.r.t. axis of rotation of the polygon. As a result, the laser beam is deflected in such a way that it moves over a section of a conical skirt, as can be seen in fig. 5.7a. This conical skirt forms a heavily bowed scan line on the wafer surface. This scan line is in the shape of a circular arc section, with the deflection point at its center, and the radial scan distance as its radius. In practice the shape slightly deviates from a circular arc section due to a deflection point shift, this will be covered in sec. 4.5.1. The polygon rotates at a constant angular velocity, the laser spot at the inspection site subsequently also moves over the wafer surface at a constant velocity.

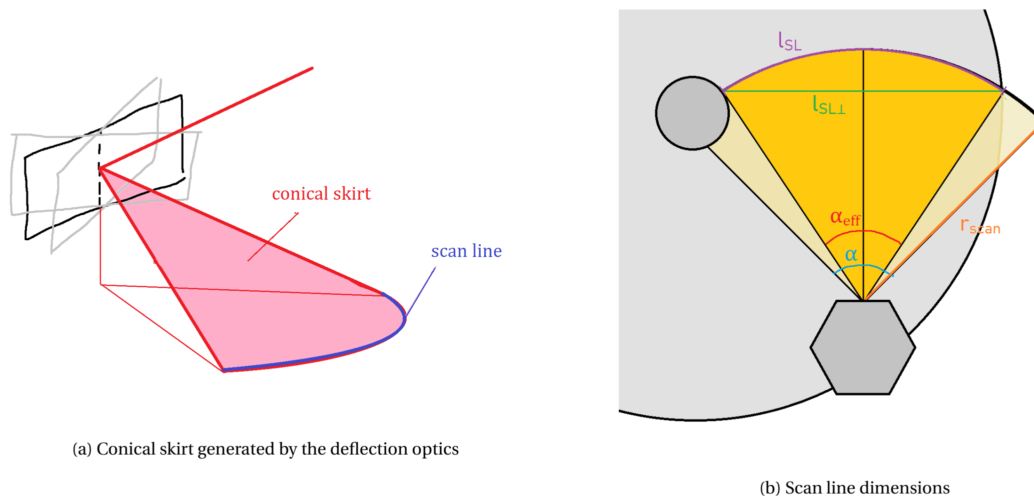

(a) Conical skirt generated by the deflection optics

(b) Scan line dimensions

Figure 4.4: An illustration of the initial deflection of the beam - and the generation of a scan line

The maximum scan angle that can be achieved by a polygon is twice its angle of rotational symmetry. Achieving that maximum scan angle is however not feasible in practice. In order for the laser to scan the extremities of the scan line, the laser must be incident on the very edge of the polygon facet. As the point of incidence on the polygon moves closer to the facet edge, more and more of the beam profile gets cut off, greatly reducing the beam quality. To combat this issue, only a fraction of the polygon facet will be used for measurements. This fraction will be referred to as the polygon duty cycle (D). (e.g. a polygon with 12 facets has a total scan angle of 60 deg, with a duty cycle of 0.75 that translates to an effective scan angle of 45 deg). A large duty cycle value is beneficial - since the duty cycle effectively reflects the percentage of time used for measurement - but not so large that significant cut-off occurs. A smaller duty cycle can be chosen to reduce the deflection point error as described in sec. 4.5.1, however this does not seem to be an issue for this design. The perpendicular length of a scan line ($l_{SL\perp}$) is roughly 135 mm. As shown in eq. 4.16, this length and the radial scan distance (r_{scan}) can be used to find the required effective scan angle (α_{eff}). Choosing a small value for the radial scan distance is beneficial for the design, since it will increase the NA that can be achieved for a given facet size. However choosing a small radial scan distance, also means that a large effective scan angle is required - increasing the scan line bow, and reducing the number of facets that the polygon can have, which in turn increases the required rotation speed of the polygon to create enough scan lines.

The bow in the scan line causes the real length to be greater than the perpendicular length. The length of a scan line (l_{SL}) can be expressed in terms of the scan distance (r_{scan}) and the effective scan angle (θ_{eff}), as shown in eq. 4.15.

$$l_{SL} = r_{scan}\,\theta_{eff} \tag{4.15}$$

$$\alpha_{eff} = 2\,\arcsin\frac{l_{SL\perp}}{2\,r_{scan}} \tag{4.16}$$

4.3.2. Spot size, pixel size, and bandwidth

While the rotating polygon deflects the beam in the scan direction to generate scan lines, the wafer rotates underneath the scan lines in the cross-scan direction to give these scan lines separation on the wafer surface. The combination of these two motions creates the raster scanning pattern, that covers the entire wafer surface. Because of the constant angular velocity of the wafer, each scan line has a constant separation d_{SL} from the previous one (cross-scan direction) at the wafer edge. On each of these scan lines, multiple data points are taken, each separated by distance d_{pix}. The pixels at the edge of the wafer are of size $d_{SL} \times d_{pix}$, and get smaller in the cross-scan direction as you move closer to the P-chuck. When the pixel size is mentioned in this report, the maximum $d_{SL} \times d_{pix}$ is what is referred to.

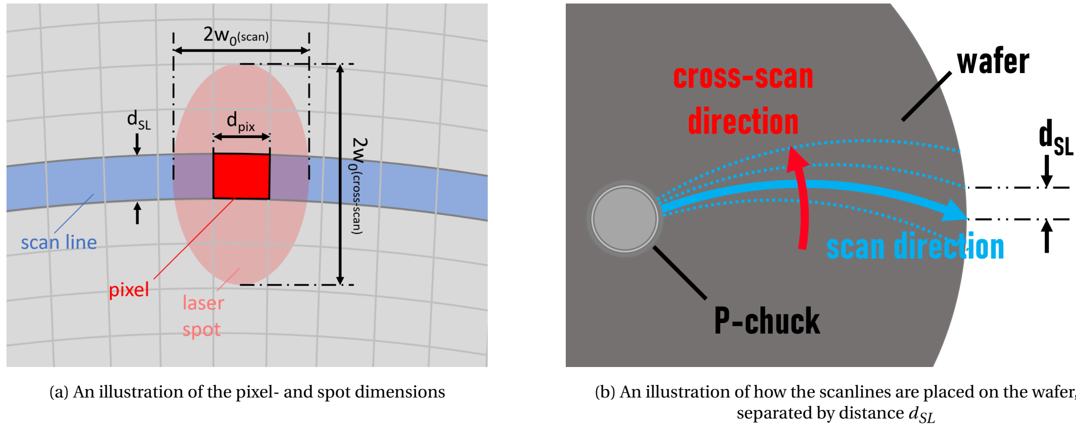

(a) An illustration of the pixel- and spot dimensions

(b) An illustration of how the scanlines are placed on the wafer, separated by distance d_{SL}

Figure 4.5

The pixel size should not be confused with the spot size. The pixel size is determined by where the samples are taken - and the spot size is the actual size of the laser beam incident on the wafer during those measurements. As the laser beam is incident on the wafer under an angle, the resulting spot is elongated in the cross-scan direction. The result is that the spot is of an elliptical shape. The incident angle determines how much the spot is stretched. We characterize the spot size with separate $2w_0$ values in the respective directions. In our design we choose the spot size to be much larger than the pixel size. This guarantees that when a droplet is measured, there is always a pixel in which it is located in a high intensity section of the spot. This avoids the signal variation - and thus the chance that a droplet is missed. This signal variation as a result of pixel- and spot size is calculated in sec. 4.5.

With the pixel size, and the wafer dimensions, we can easily find the total pixel count (n_{pix}), which is required for finding the measurement bandwidth. The measurement bandwidth (B) is one of the limiting factors of the design, since the amplitude of the frequency response of photodiodes drops above a certain frequency. Typical high-speed photodiodes have a 3db bandwidth (i.e. bandwidth where the frequency response amplitude has dropped by 50 percent) between 1 and 100 MHz. The analog circuitry could potentially limit the achievable bandwidth even further, however this is considered to be outside the scope of this research. Although values of bandwidths above these values have been found in literature, the conservative upper bound of 20 MHz is chosen to make sure the design is realistic.

The formula for the measurement bandwidth is given as:

$$B = \frac{n_{pix}}{Dt} < 20\,\text{MHz} \tag{4.17}$$

The bandwidth is not only important for this upper bound however, it also influences the signal-to-noise ratio, as will be explained in sec. 4.6.

4.4. Signal strength

The signal strength is defined to be the average current that is generated in the photodiode by the a droplet with the threshold diameter. Comparing the signal power to the noise power, the signal leak power and the signal variation, will make it possible to quantify the reliability of our measurements. To determine the signal power, we must first know how much light is incident on a droplet. Then we must investigate how this light will be scattered. Next we must calculate which FOV from the droplet to the detector, so we know which section of the scattering profile is captured. We can then use the properties of the sensor and its circuit to determine what current will be generated for the amount of light reaching the detector.

4.4.1. Incident light intensity

The spot size is an important parameter for calculating the light intensity incident on a droplet at the measurement site. As mentioned previously in sec. 4.3.2, due to the incident angle we have two separate $2w_0$

values describing the spot. The value of $2w_0$ *(scan)* is a design choice. However choosing a spot size, automatically also chooses a Rayleigh length and a beam divergence. The spot size must be chosen carefully, since it determines the spot size on other components, such as the polygon and the obstruction. A large divergence means a large spot on the polygon and the obstruction. When the beam gets too large on the polygon it can be cut off by the edge, greatly reducing the beam quality. A large spot on the obstruction also means that the obstruction must be larger to block the beam fully - reducing the amount of scattered light that can reach the detector. A small divergence however means a larger focal depth. If the focal depth is too large, the cylindrical mirror will be in focus, causing the surface inspection tool to not only measure the wafer - but also its own mirror. How much larger the $2w_0$ *(cross-scan)* is will be determined by how much horizontal power the cylindrical mirror gives the beam - and by the angle of incidence of the beam on the wafer.

A droplet at the center of a pixel will experience a higher intensity illumination than a droplet at the edge of a pixel. Equation 4.11 shows how the light intensity is distributed within a beam. We can use this equation to calculate the intensity droplets will see at our inspection area. A droplet at the center of a pixel ($r = 0$) will see the maximum illumination (I_{max}), and a droplet at the corner of a pixel $\left(r_{WC} = \sqrt{(\frac{d_{SL}}{2})^2 + (\frac{d_{pix}}{2})^2}\right)$ will see the minimum illumination. In practice the minimum illumination is even lower, since scan line errors caused by facet-to-axis angle errors (as explained in sec. 4.5.1) of the polygon add to the scan line separation. The maximum and minimum intensities are then:

$$I_{max} = I_0 \tag{4.18}$$

$$I_{min} = I_0\, exp\left(\frac{-2r_{WC}^2}{w_0^2}\right) \qquad \text{with} \qquad r_{WC} = \sqrt{\left(\frac{d_{SL}}{2} + \epsilon_{fta}\right)^2 + \left(\frac{d_{pix}}{2}\right)^2} \tag{4.19}$$

The average of these two illumination values gives us the average intensity of the incident light, and the fractional difference between the average and the extremities gives us the intensity variation. The real variation of the signal will be even larger due to other errors. However those variations are repeatable - and can be compensated for. This will be discussed in sec. 4.5.

4.4.2. Scattering profile

The light that is incident on a droplet will scatter in all directions. How the scattered light is distributed is described by the scattering profile. Light scattering is a complex phenomenon, and is dependent on many factors, such as droplet size, droplet shape, and angle of incidence. Because of the large number of assumptions, it is not very likely that a simulation of the scattering process will be fully representative of reality. However, the results of a simulation can give a rough idea of the signal we can expect. Eventually system will be calibrated to measure the correct size.

A 2D geometric optics simulation was set up in Matlab. In this simulation a collimated beam of constant intensity is incident on a perfectly spherical droplet. For each ray the simulation stores the how much power is scattered in which direction. Only the angular data is stored, i.e. the scattering droplet is considered to function as a point source. Because this model is rotationally symmetric, the resulting 2D scattering profile can be rotated along the optical axis to extrapolate to a 3D scattering profile. A plane is added, that is coincident with the wafer surface. The part of the scattering profile that lies below this plane (i.e. the dark side of the wafer) is fully reflected over this plane. The resulting scattering profile, is the three dimensional scattering profile of an ideal hemispherical water droplet, on a ideal flat fully reflective surface, when perfectly collimated light is incident under angle α.

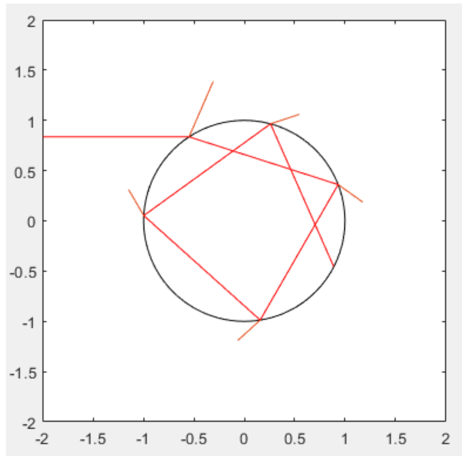

(a) Illustration of one ray of the geometric optics simulation, at each air-water interface the the total remaining power in the beam is split up in a reflected- and refracted part according to the Fresnel equations. The part that exits the droplet is stored in a bin corresponding to its angle (in steps of full degrees). This is repeated until only a certain fraction of the original beam power is left, or after it exceeds a bounce limit. This process repeats for every ray.

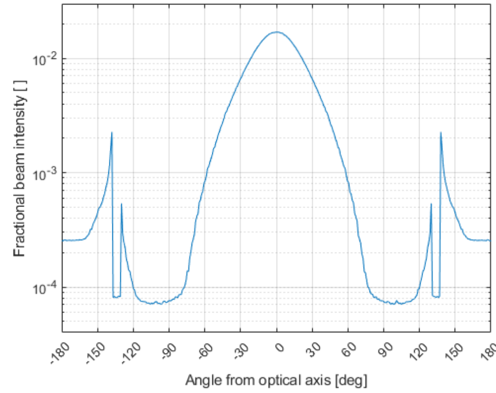

(b) 2D-scattering profile that yields from the simulation, plotted logarithmically

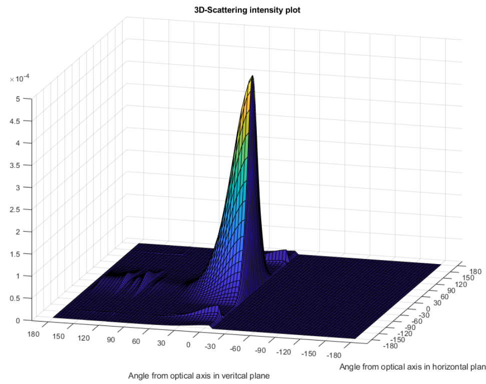

(c) 3D-view of the scattering profile after reflection over a plane

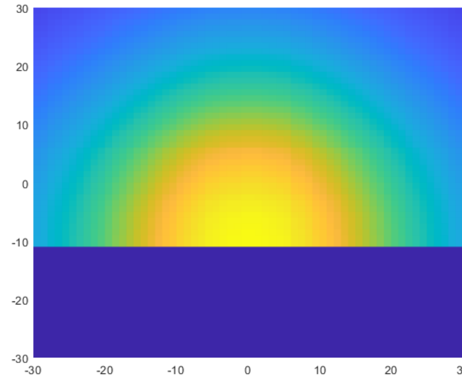

(d) Section of the scattering profile after reflection in colormap view. Numbers on the axes represent horizontal- and vertical angle from optical axis in degrees.

Figure 4.6

4.4.3. Field of view to collection optics

Combining the light intensity incident on the inspection site from sec. 4.4.1 and the dimensionless scattering profile from sec. 4.4.2 allows us to assign quantitative intensity values to the scattering profile. Now we must find out what the field of view is from the inspection site to the detector. Integrating the scattering profile over this field of view (FOV) will yield the total power of the light reaching the detector.

By selecting the correct lenses for the collection of light, it is possible to focus all the scattered light that reaches the polygon facet on the detector. By assuming that we can find this correct lens, we can greatly simplify the calculation - now only the FOV from the inspection site to the polygon facet must be found. This FOV is a function of the angle of incidence (α), the gap between the wafer and the polygon (h_{pol}), the height of the polygon facet (h_{facet}), the length of the polygon facet (l_{facet}) and the radial scan distance (r_{scan}). The The FOV can be divided up in a horizontal, and vertical component. For a datapoint at the midpoint of the scan line the FOV is described by the following equations:

$$FOV_{hor,m} = \left[-\arctan\left(\frac{0.5l_{facet}}{r_{scan}}\right), \quad \arctan\left(\frac{0.5l_{facet}}{r_{scan}}\right)\right] \tag{4.20}$$

$$FOV_{ver,m} = \left[\arctan\left(\frac{h_{pol}}{r_{scan}}\right) - \alpha, \quad \arctan\left(\frac{h_{pol}+h_{facet}}{r_{scan}}\right) - \alpha\right] \tag{4.21}$$

The vertical FOV remains constant over the entire scan line. The horizontal FOV will however slightly change for different data points on the scan line. This is further elaborated in sec. 4.5.2. The average of the FOV at the edge, and the FOV at the center of the scan line is used to find the signal strength.

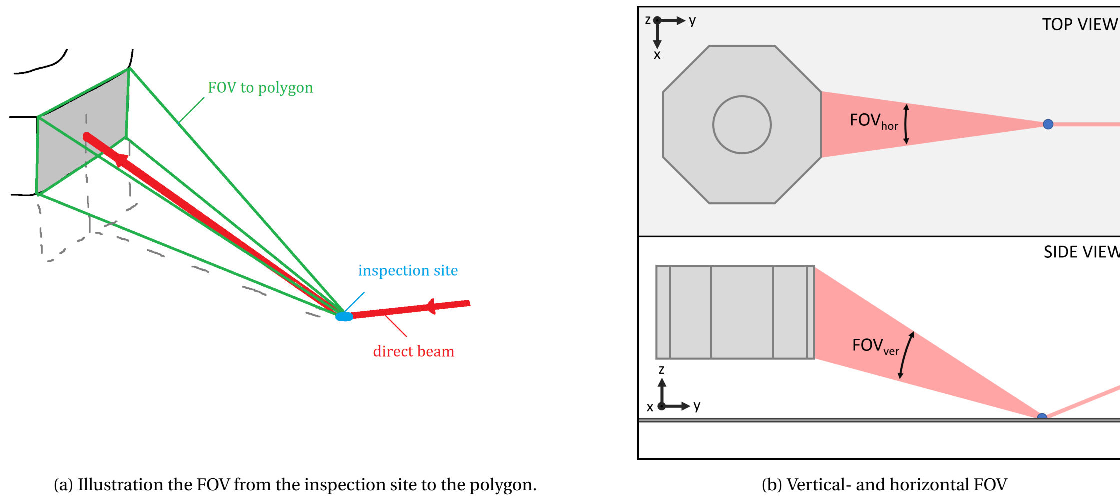

(a) Illustration the FOV from the inspection site to the polygon.

(b) Vertical- and horizontal FOV

Figure 4.7

4.5. Signal variation

The signal variation is a measure that quantifies the amount of deterministic variation that is expected for a measurement of a droplet of a constant size and shape. The signal variation can be divided up into repeatable, and non-repeatable variation. Non-repeatable variation can not be corrected for, and is accounted for in the type 1- and 2 error rate calculations. Repeatable errors are described and calculated, but are not incorporated in the error rates, since they can be accounted for. There are three sources of signal variation: 1) Illumination variation, 2) field-of-view variation and 3) scattering profile variation.

4.5.1. Illumination variation

When the illumination of a droplet varies, so does the signal. The two main ways in which the illumination a droplet experiences can vary are: 1) droplet (transverse) location within spot, and 2) defocus of the beam.

Droplet location within spot

As was already discussed briefly in in sec. 4.3.2, where a droplet is located in a spot has a large effect on the illumination of the droplet. There are several factors that cause the spot to move - some are problematic - and others cancel out. The scan line errors that will be discussed are: 1) wafer warp error, 2) polygon deflection point error, 3) polygon wobble error and 4) polygon facet-to-axis angle error

1) Wafer warp error: The wafer is only fixated at the center by the P-chuck, a large portion of the wafer is unsupported, and wafer warp that is either naturally present in the wafer - or that is a result of gravity cause the wafer to warp in the shape of a saddle. The peak-to-peak error at the edge of the wafer can be as high as 450 µm. At first inspection this sounds like a problematic error. With a very low angle of incidence this can error can cause a displacement of the scan line of up to a few millimeters. However on further inspection one can see that the peaks are a quarter of a wafer rotation apart - spreading this large error over many scan lines. The scan line-to-scan line component of this error is negligible, since the exact location of our pixels is not relevant.

2) Polygon deflection point error: The deflection point on the polygon is treated as stationary. However, when comparing a polygon to its inscribed circle, one can see that the deflection point moves forward as the induced angle on the beam increases. This error does not cause an angular error - but it does introduce a horizontal displacement error in the direction radially outwards from the axis of the polygon in the direction of the deflection point, as illustrated in fig. 4.8b. Depending on the polygon facet count and facet length, this

can be an error as large as several millimeters. However, since the same applies to every scan line, the scan line-to-scan line component of this error is negligible.

3) Polygon wobble error: Polygons experience some wobble due to imperfections in the bearings and motor. Because this is an angular error with respect to the axis of the polygon, there is a vertical component that introduces scan line errors in the cross-scan direction. The polygon wobble is specified by the manufacturer, and the values they guarantee are usually between 5 and 60 arcsec. The frequency of this error is not specified, however we expect the peaks of the error to be at least half a polygon rotation apart. This means that the error is spread over several scan lines, however due to the low angle of incidence the angular error is magnified. This error is not negligible, however this error can be minimized by selecting a polygon with a low wobble.

4) Polygon facet-to-axis angle error: Due to the manufacturing tolerances there is always some error in the angles of the polygon faces. Errors in angles in the plane of rotation (i.e. causing scan line errors in the scan direction) can be compensated for with a start-of-scan diode. However angular errors with respect to the axis cause discrete jumps of the scan line in the cross-scan direction between scan lines. This error is very problematic. This error is specified by manufacturers. Additionally manufacturers often specify a tighter tolerance for the polygon facet-to-axis angle error between adjacent facets. This can be used to calculate the maximum jump that can occur between adjacent scan lines. This error has typical values around 1 arcsec.

Scan line errors in the cross-scan direction as a result of angular errors w.r.t. the axis of the polygon, such as the wobble error and the facet-to-axis angle error, are a function of the height of the deflection point (h_{DP}), the angle of incidence (α) and the angular error w.r.t. the polygon axis (δ_α)can be found with the following equation:

$$\epsilon_{fta} = h_{DP} \tan\left(\frac{\pi}{2} - \alpha + \delta_\alpha\right) - h_{DP} \tan\left(\frac{\pi}{2} - \alpha\right) \tag{4.22}$$

Eq. 4.19 can be used to find the illumination variation as a result of droplet location within the spot.

Defocus errors
As can be derived from the equations in sec. 4.2 defocus of the beam causes a variation of illumination intensity. The factors that cause defocus errors in this design are: 1) the low angle of incidence and 2) the wafer warp.

1) Low angle of incidence defocus: The low angle of incidence causes a larger section of the propagation distance to be used for inspection. For angle of incidence (α) and transverse minimum beam waist ($2w_0$) the defocus (Δz_α) is:

$$\Delta z_\alpha = \frac{w_0}{\tan(\alpha)} \tag{4.23}$$

2) Wafer warp defocus: The warp of the wafer causes defocus alongside the previously mentioned scan line errors. The defocus as a result of wafer warp is a function of the vertical wafer warp deflection (δh_{warp}) and the angle of incidence (α), and can be found with the following equation:

$$\Delta z_{warp} = \frac{\delta h_{warp}}{\sin(\alpha)} \tag{4.24}$$

These defocus contributions can be filled into eq. 4.14 to find the change in beam waist, which can subsequently be filled into eq. 4.11 to find the change in illumination as a result of defocus.

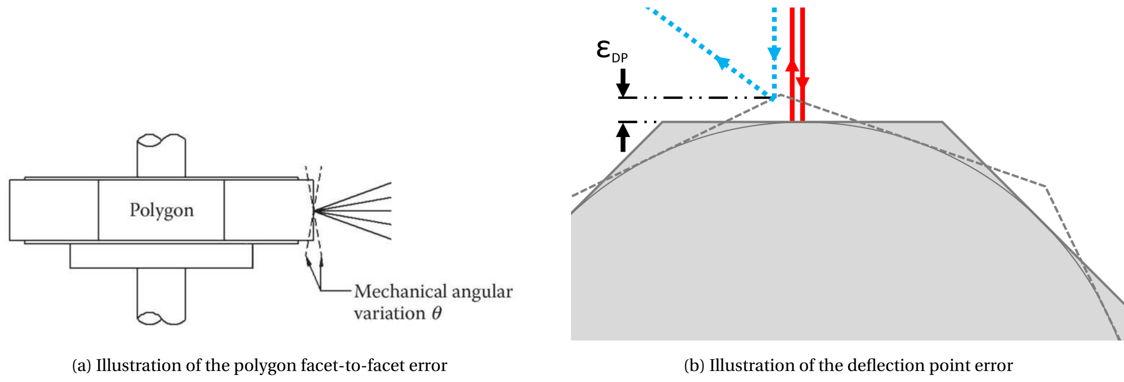

(a) Illustration of the polygon facet-to-facet error

(b) Illustration of the deflection point error

Figure 4.8

4.5.2. Field-of-view variation

As mentioned previously, the field-of-view from the droplet to the detector varies with the deflection angle of the polygon. At the edges of the scan line there will be a different FOV then at the center of the scan line. There are two factors contributing to this FOV shift: 1) Rotating the polygon by an angle will impose twice that angle on the outgoing beam. This means that the facet will only be perpendicular to the outgoing beam at the midpoint of the scan line. This angle will slightly decrease the effective facet size, however this effect is very small for small angles. 2) The location of the deflection point on the polygon facet will change when scanning different points on the scan line. When taking a data point at the edge of the scan line, the deflection point must likewise move to the edge of the effective facet (i.e. the edge of the facet within the duty cycle). Fig. 4.8b can help understand this. This effect will not affect the total FOV angle, it will however shift where its center will be on the facet. This can have a significant effect on the signal, since the scattering profile is centered around the deflection point. These errors are repeatable however, so they can be corrected for. Solving this problem analytically got quite messy and complicated - since this is not a very important factor, the calculations have been performed numerically.

4.5.3. Scattering profile variation

One of the major benefits of this design is that the angle of incidence stays constant for all data points. This means that the variation of incident angle can not have an influence on the scattering profile. The shape of the droplets does however still affect the scattering profile. A difference in hydrophobicity of the surface, impact force of the droplet deposition and interaction with other droplets can possibly affect the shape of the droplets. Smaller droplets however tend to be more spherical - since surface tension becomes the dominant force on those length scales. Large droplets are expected to give signals with much higher amplitudes, regardless of their shape. It is assumed that droplets near the threshold diameter do not vary significantly in shape. This should however be verified experimentally, since the performance of the system relies on it.

All variations are calculated as percentages. The relevant contributions are combined multiplicatively, so that one number for the signal variation remains.

4.6. Noise power

The noise is the last piece of the puzzle we need to calculate the system performance. There are several relevant noise sources for an optical system like this. Thermal noise, shot noise and dark current noise are the most important contributors. Due to a lack of time we have chosen to estimate the noise power through the use of the sensor Noise Equivalent Power (NEP). The NEP of a sensor is the minimum detectable power of a sensor, given as a function of the bandwidth. The NEP can be used to estimate the noise in a system in the following way:

$$P_{noise} \approx NEP(\lambda)\sqrt{BW} \tag{4.25}$$

It should be noted that this is only true when the signal power is equal to the noise power. The signal power we use will be much higher than the noise power, so this estimate for the noise is probably on the low side.

Then finally, we can calculate if the system meets the type 1- and type 2 error rate requirements. The signal

amplitude of a 45 μm droplet is calculated, and the worst-case negative signal variation is found and subtracted. The amount of current that is still remaining before the threshold current is crossed, is the amount of current that must be generated by noise to achieve a false negative measurement. Similarly, the signal amplitude of a 25 μm droplet is calculated, and the worst-case positive signal variation is added. The amount of current that is still remaining before the threshold current is crossed, is the amount of current that must be generated by noise to achieve a false positive measurement. We use these values to calculate Z-values to put into a cumulative distribution function to find the chance of the respective errors occurring. As stated earlier, the Z-values can get pretty high for this calculation, and it is unclear if the result is even meaningful. However, the high Z-values indicate that the system will work very well.

4.7. Circular obstruction

The dark field illumination relies on a the circular obstruction preventing the direct beam from reaching the detector. Due to the Gaussian nature of beams, some electromagnetic radiation will always pass - however if we choose the circular obstruction large enough, this effect will be negligible. Choosing a circular obstruction that is twice the size of the beam diameter does not suffice however. Several errors in the system cause the returning beam to move. The obstruction should be large enough that these movements do not cause the direct beam to leak to the detector. The previously mentioned errors that contribute to movement on the obstruction are: 1) the angular polygon wobble error, 2) the angular facet-to-axis angle polygon error, 3) the vertical displacement error caused by wafer warp and 4) the vertical component of the deflection point error. Additionally the wafer warp also has an angular component, that can be found by evaluating the steepest angles we find when imposing a sine wave with an amplitude of 225 μm on the edge of the wafer. Furthermore, the deflection point error also causes a slight misalignment with the cylindrical mirror, which then imposes an angular error on reflection. If this error would be too large, the cylindrical mirror can be replaced with a freeform mirror that corrects for the deflection point error. However, that does not seem to be necessary since the error is only in the order of a few mrad.

The angular errors are multiplied with the distance from where the error occurs to the obstruction to find their displacement value. Horizontal displacements and vertical displacements are added separately, and the square root of the sum of their squares is calculated to find the maximum radius of the spot displacement. The full minimum beam waist ($2w_0$) is added to this radius to ensure that virtually none of the signal passes the obstruction. The equation for the minimum radius of the obstruction is then given as:

$$r_{obst} \geq \sqrt{\left(\sum \delta_{hor}\right)^2 + \left(\sum \delta_{ver}\right)^2} + 2w(z_{obst}) \tag{4.26}$$

4.8. Contamination of optical components

Although the system will be designed in such a way that contamination of the measurement equipment will be reduced to a minimum, there is a possibility that water droplets or dust particles get deposited on our measurement equipment. It is good practice to design the system in such a way that it is insensitive to these sorts of contamination. We can do this by making sure that the surfaces of reflecting components are out of focus. By the nature of this design, the cylindrical mirror is very close to the inspection site. This is one of the weaknesses of this design. If the cylindrical mirror is fully in focus, we are effectively inspecting the mirror surface too.

Firstly, we can reduce this effect by increasing the distance between the mirror and the inspection site. We cannot increase this distance freely though. As the cylindrical mirror moves further away from the inspection site, the vertical distance between the incoming- and outgoing spot on the polygon increase as well. This increases the required facet height, which is likewise something we cannot increase indefinitely.

Secondly, we can increase the divergence of the beam. This will cause the spot to be larger, and thus the intensity to be lower on the mirror surface. Increasing the beam divergence can be achieved by choosing a large wavelength of light, or a small spot size. A smaller spot size will however also increase the signal variation - giving rise to another trade-off.

To guarantee some robustness to contamination of the cylindrical mirror, we include the background signal of a droplet of 35 μm on the cylindrical mirror in the error rate calculation. However larger droplets contaminating the optical components is not guaranteed to leave the performance unhindered. It should be investigated how clean these components can stay in this environment.

4.9. Parametric design tool

This design has many parameters that all cooperate to yield a certain system performance. Judging whether a design parameter is good in isolation, is very difficult. To make the design process easier, a parametric A parametric design tool has been developed in Excel. This tool contains all the equations described in this report, and links them so that the design choices can be used as inputs, and the tool calculates the performance automatically. This tool is very useful for getting a better understanding of the nuances of the design - and for tweaking the design parameters to find an optimal design. Asides from the performance, the design tool also calculates important dimensions of the scanner geometry and its components, and automatically adjusts the values in an overview picture of the setup - making it easier to recreate parts in 3D-CAD software. Fig. 4.9 and 4.10 show some images of this parametric design tool.

First Principles Design

Design parameters

Name	Fill in		SI		Remark
(2*W0) spot size	100	µm	1.00E-04	m	Perpendicular to propagation direction
Measurement time	2.00	s	2.00E+00	s	
Incident angle	1/5		1.97E-01	rad	[ver/hor] - Manually change polynomial coefficients that yield from geometric_scattering_profile_intensity_profile.m (right of Performance)
Radial scan distance	90	mm	9.00E-02	m	Horizontal distance between deflection point and arbitrary point on scanline
Scanline separation (cross-scan direction)	180.00	µm	1.80E-04	m	
Pixel separation (scan direction)	25.00	µm	2.50E-05	m	
Maximum facet count	9		9.00		
Polygon facet count	8		8.00E+00		
Minimum facet length	7.47	mm	7.47E-03	m	In order to achieve duty cycle with 2spot roll-off
Facet length	40	mm	4.00E-02	m	
Minimum facet height	20.38	mm	2.04E-02	m	In order to have outgoing and incoming beam with 2spot roll-off
Facet height	30	mm	3.00E-02	m	
Light wavelength	632	nm	6.32E-07	m	(Manually change silicon reflectivity after changing)
Scanline - Mirror offset	45	mm	4.50E-02	m	
Mirror correction	NO		0		[1 = YES 0 = NO] Replace cylindrical mirror for a freeform mirror to negate the horizontal component of the deflection point error
Minimum obstruction diameter	10.23	mm	1.02E-02	m	
Obstruction diameter	11.00	mm	1.10E-02	m	
Minimum collection optics / obstruction distance	168.27	mm	1.68E-01	m	
Collection optics / obstruction absolute distance	180.00	mm	1.80E-01	m	
Minimum silvered mirror horizontal distance	52.50	mm	5.25E-02	m	In order to hit facet in center, possible to ignore this
Silvered mirror horizontal distance	55.00	mm	5.50E-02	m	
Sensor NEP	3.00E-15	W/Hz^(1/2)	3.00E-15	W/Hz^(1/2)	
Laser power	35.00	mW	3.50E-02	W	
Polygon facet-to-axis angle error	1.00	arcsec	4.85E-06	rad	
Estimated component reflectivity	90.00	%	9.00E-01		

Calculations

Name	Value		SI		Remark
Pixels, scanlines and bandwidth					
Pixel count per scanline	5.25	x10^3	5.25E+03		
Scanline count	5.24	x10^3	5.24E+03		
Total pixel count	27.49	x10^6	2.75E+07		
Bandwidth	17.13	MHz	1.71E+07	Hz	(Peak BW - including duty cycle)
Beam properties					
Radial beam divergence	4.02	mrad	4.02E-03	rad	Radial, so half of full divergence
Rayleigh length	12.43	mm	1.24E-02	m	DOF = 2x Rayleigh
Spot size on wafer - long	509.90	µm	5.10E-04	m	Spot size in the cross-scan direction
Spot size on wafer - short	100.00	µm	1.00E-04	m	Spot size in the scan direction
Polygon dimensions and placement					
Absolute scan distance	91.78	mm	9.18E-02	m	Absolute distance between deflection point and arbitrary point on scanline
Required radial scan angle	72.20	°	1.26E+00	rad	
Polygon facet-facet angle	45.00	°	7.85E-01	rad	
Theoretical maximum radial scan angle	90.00	°	1.57E+00	rad	
Polygon duty cycle	0.80		0.80		
Facet roll-off distance	3.96	mm	3.96E-03	m	
Returning beam spot diameter on DO	0.74	mm	7.39E-04	m	
Outgoing beam spot diameter on DO	1.48	mm	1.48E-03	m	
Returning spot offset on DO (constant)	18.00	mm	1.80E-02	m	Result of cylindrical mirror offset
Returning spot offset on DO(variable)	0.90	mm	9.00E-04	m	Result of wafer warp (worst case)
Polygon inscribed radius	48.28	mm	4.83E-02	m	
Polygon placement height	12.00	mm	1.20E-02	m	(offset between polygon and wafer)
Polygon rotation speed	19635	rpm	2.06E+03	rad/s	
Stress in polygon	8.90	MPa	8.90E+06	Pa	
Error contributions for spot movement on					
Deflection point error	2.60	mm	2.60E-03	m	Distance the polygon moves 'out' worst case scenario (beginning/end scanline)
Vertical shift of spot on DO due to deflection point error	0.51	mm	5.09E-04	m	In- and outgoing beam relative vertical movement due to deflection ponit error making the path shorter
Curvature mirror	7	1/m	7.41E+00	1/m	
Angular error of cylindrical mirror due to deflection point error	11.33	mrad	1.13E-02	rad	

Ideal performance

Name	Fill in		SI		Remark
Signal power	19.93	nW	1.99E-08	W	Approximately 1E-15 J per pixel
Signal variation	15.83	%	1.58E-01		(worst case)
Background signal power	0.00	pW	2.13E-15	W	(worst case, assuming sources <10% of our feature signal)
Noise power	12.42	pW	1.24E-11	W	
S/N ratio	**32.05**	**dB**	1.60E+03		**At least 26.42 dB required**
Wafer heating	**0.49**	**mK**	4.90E-04	K	**< 0.74 mK**

Constants

Name	Fill in		SI		Remark
Wafer thickness	775	µm	7.75E-04	m	
Wafer diameter	300	mm	3.00E-01	m	
Chuck diameter	38	mm	3.75E-02	m	
Scanline length	131	mm	1.31E-01		Straight distance between the endpoints of the (curved) scanline
Wafer mass	128	g	1.28E-01	kg	
Wafer warp	450	µm	4.50E-04	m	(Peak-peak)
Silicon specific heat	700	J/(kg K)	7.00E+02	J/(kg K)	
Silicon density	2330	kg/m^3	2.33E+03	kg/m^3	
Reflectivity silicon	37.41	%	3.74E-01		
Droplet size	35	µm	3.50E-05	m	
Tensile strength aluminum	90	Mpa	9.00E+07	Pa	
Density aluminum	2710	kg/m^3	2.71E+03	kg/m^3	
One false negative allowed per	6200	wafers	6.20E+03		(Letting a droplet pass undetected)
One false positive allowed per	15	wafers	1.50E+01		(Falsely detecting a droplet)
Upper bound confusion region	45	µm	4.50E-05		
Lower bound confusion region	25	µm	2.50E-05		
Background signal feature strength on DO & cylindrical mirror	100	%	1.00E+00		

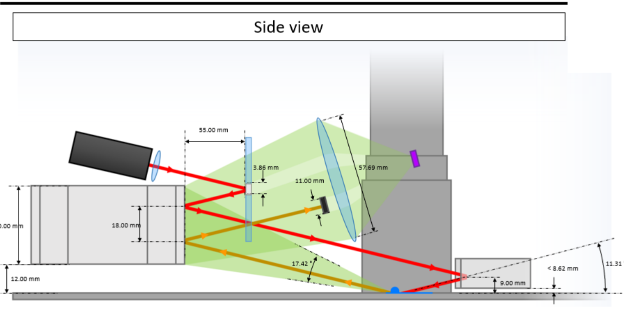

Figure 4.9: Impression of the parametric design tool (Top half).
(Only to give an impression - values may be dated!)

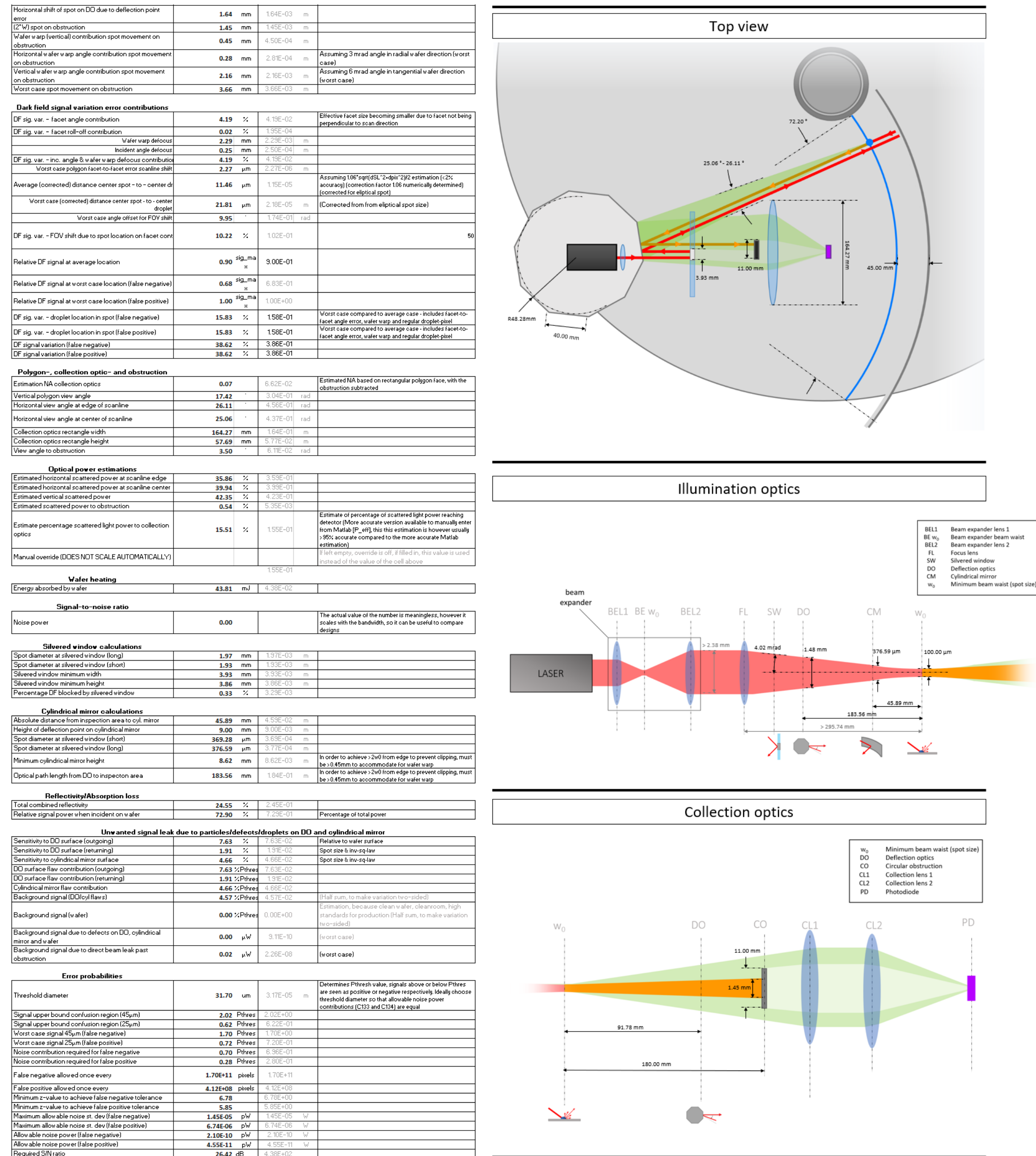

Figure 4.10: Impression of the parametric design tool (Bottom half).
(Only to give an impression - values may be dated!)

4.10. Design summary

With the use of the parametric design tool we found a design that meets the performance criteria. The important design parameters are shown in tab. 4.1, and tab. 4.2 summarizes the achieved performance.

property	value
minimum beam waist	100 µm
Rayleigh length	12.4 mm
beam divergence	4.0 mrad
pixel size ($S \times CS$)	25 × 180 µm
bandwidth	17.1 MHz
incident angle	11.3°
radial scan distance	90 mm
polygon facet size ($h \times l$)	25 × 30 mm
polygon facet count	8
polygon inscribed radius	36.2 mm
polygon rotation speed	19600 rpm
polygon duty cycle	0.8
cylindrical mirror offset	40 mm
cylindrical mirror radius	90 mm
obstruction diameter	11 mm
laser power	35 mW
laser wavelength	632.8 nm

Table 4.1: Summary of the properties of the design

property	value	
signal power	8.8 nW	
signal variation	<15.8%	
noise power	12.4 pW	
measurement time	2	≤ 2 s
SNR	28.5 dB	≥ 26.4 dB
wafer heating	0.49 mK	≤ 0.74 mK

Table 4.2: Summary of the performance of the design

5
Experimental validation

To make sure the design is feasible we must perform some experimental validation for our theoretical design. Building and testing an experimental setup can reveal new problems, uncover wrong assumptions and show where the practical world deviates from theory.

5.1. Goals experimental validation

The ultimate goal of experimental validation is building a full prototype of the machine, and testing it to show that it meets the performance requirements. However building a full prototype is challenging, and a large investment in both time and money. It requires buying expensive components, and many hours of building, alignment and testing. There is a very realistic chance that the prototype reveals some issue that was not accounted for in the theoretical design. To prevent wasting a lot of time and money, some subgoals have been set up.

The following subgoals have been selected:

- Show proof of concept
- Build simplified scanner and test its performance
- Characterize scattering behavior - and compare it to the model
- Build a full prototype and test its performance

5.2. Preliminary testing: Proof of concept

Before even starting the first principles design, we wanted to make sure that the working principle of the concept was feasible. To show proof of concept, a very primitive test setup was build - and some preliminary testing was performed. A water droplet was deposited on a wafer fragment, and the wafer fragment was placed in a relatively dark enclosure. Some graph paper was placed on both the floor and back wall of the enclosure to keep track of the distances. A regular laser pointer is mounted in such a way that it is incident on the droplet under an angle. By visually inspecting the light that reaches the graph paper on the back wall, we can get a rough idea of the scattering profile.

To ensure that the scattering profile shows up clearly enough to do the inspection visually, we chose droplets of around 1-2 mm in diameter. Although this is much larger than the droplets that we are interested in, we expect the angular scattering distribution to be unchanged - only higher in amplitude. Both the droplets we use for this experiment, and the droplets we are interested in eventually are in the geometric scattering regime. Only when droplets get much smaller, and enter the Mie- or Rayleigh scattering regime, the angular scattering distribution will drastically change. Droplet size can however affect the droplet shape slightly, which will affect the scattering profile, this effect is neglected for now.

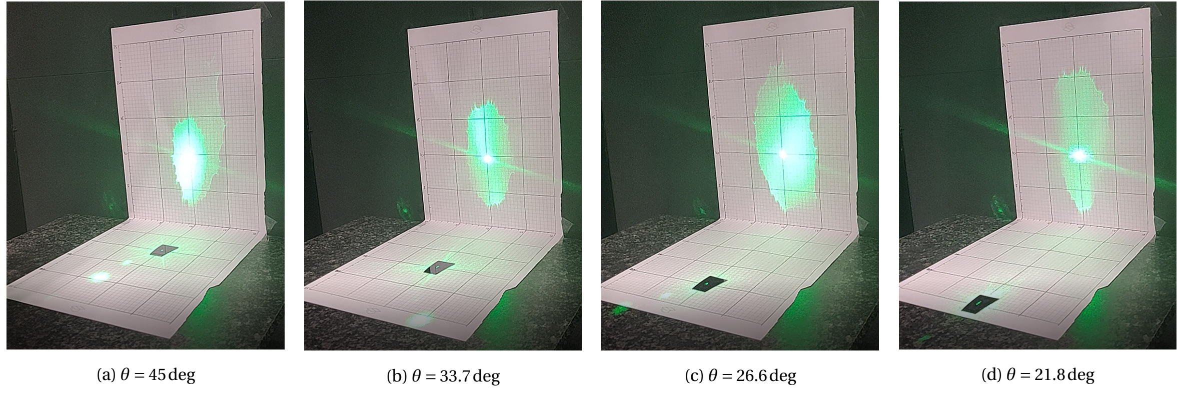

(a) $\theta = 45\,\text{deg}$ (b) $\theta = 33.7\,\text{deg}$ (c) $\theta = 26.6\,\text{deg}$ (d) $\theta = 21.8\,\text{deg}$

Figure 5.1: Preliminary testing, to show if droplets scatter light as we expect. The light is incident under angle θ. The graph paper is A4 sized, with square blocks of 5cm x 5cm marked on them.

Characterizing the entire scattering profile visually will be difficult. We can however see a clear boundary of the the central lobe of the scattering profile. This central lobe in the profile is caused by lensing of the droplet. We can analyse the profile on the graph paper on the back wall, and determine the angle between the central lobe, and the axis of propagation of the direct beam. Four angles will be measured, as illustrated in fig. 5.2.

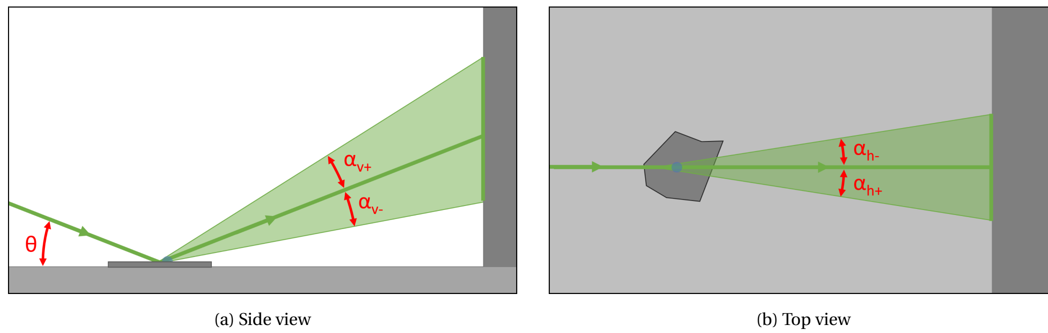

(a) Side view (b) Top view

Figure 5.2: Two views of the setup for preliminary testing.

Central lobe angular profile preliminary testing

	α_{v+}	α_{v-}	α_{h+}	α_{h-}	$\alpha_{v,full}$	$\alpha_{h,full}$
$\theta = 45.0°$	11.3°	27.0°	8.0°	10.0°	38.3°	18.0°
$\theta = 33.7°$	14.9°	22.4°	9.4°	9.4°	37.3°	18.8°
$\theta = 26.6°$	20.5°	20.1°	11.4°	10.1°	40.6°	21.5°
$\theta = 21.8°$	17.6°	17.2°	-	-	34.8°	-

Table 5.1: Results of the preliminary experiments, the two missing values are caused by the last measurement not fully illuminating the droplet, causing only a fraction of the scattering profile to show

From the results of the preliminary experiment we can see that the central cone of the scattering profile behaves relatively predictably. The full angle of the central lobe of somewhere between 20 and 40°. From perfectly hemispherical droplets, we expect the profile to be the same in the horizontal and vertical direction, that is clearly not the case here. The divergence of the central lobe of the scattering profile is much larger than the horizontal one.

The concept seems very feasible judging only from this simple experiment. The frontal lobe is bright, and relatively narrow, but not so narrow that it becomes difficult to separate the direct beam from the scattered light.

5.3. Experimental setup

With a limited budget, and limited time, we decided to simplify the prototype by leaving the cylindrical mirror out and by using as many components that were at hand. This greatly reduced the cost and made building the setup much easier.

The scanning motion is generated with a 1-axis galvanometer mirror attached to a function generator running a sine wave at a 100 Hz. The amplitude of this sine wave is tweaked until a scan line on the wafer fragment of approximately 5 mm is reached.

The cross-scan motion is generated with a manual single-axis micrometer stage. The stage will be moved in increments of 12.5 µm between measurements.

The lack of cylindrical mirror means that the prototype cannot use synchronous scanning. Because the returning beam will not be stationary, the circular obscuration must be replaced with a strip along the entire scan path. This obscuration is formed by simply placing a piece of black duct tape over the center of the lens. The piece of tape that is used was roughly 5 mm in height.

In the experimental setup, a He-Ne laser of 1.2 mW, beam diameter of 0.7 mm, and wavelength of 632.8 nm was used. A beam expander is formed from an f=10mm and an f=40mm achromatic doublet lens, placed 50mm apart. This expands the beam to roughly 2.8 mm, before being focused by a lens with an f=150 mm achromatic doublet. The beam is focused to a spot with a beam waist of roughly 43 µm.

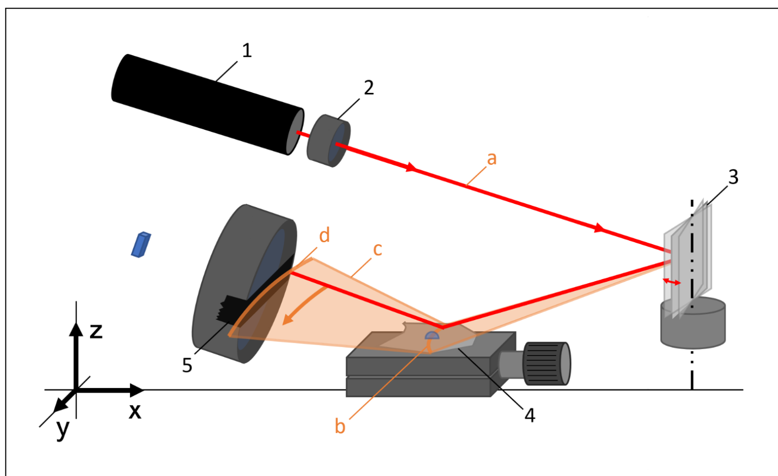

(a) An illustration of the scanning geometry of the experimental setup

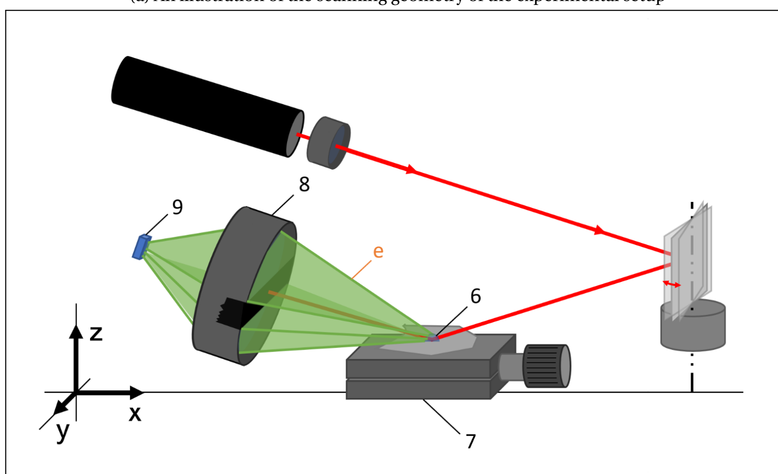

(b) An illustration of the light collection of the experimental setup

1) 1.2 mW He-Ne laser source
2) beam expander and focus lens
3) 1-axis galvanometer mirror running at 100 Hz
4) silicon wafer fragment
5) obstruction strip formed by black duct tape of height 5mm
6) deposited sunflower oil droplet
7) manual single-axis micrometer stage
8) 1 inch f=40mm doublet lens
9) BWP34 photodiode

a) direct laser beam
b) scan line on wafer fragment
c) reflected conical section shows the path the deflected laser beam follows
d) path of direct beam on the obstruction

Figure 5.3: The experimental setup explained in two images, the first image shows the light path of the direct laser beam, the second image shows how the scattered light reaches the detector.

After the direct beam is blocked, the scattered light is then focussed on the photodiode with a stack of a f=125 mm- and a f=40 mm achromatic doublet.

A BWP34 photodiode was chosen because it was readily available. The photodiode is placed in the crude

circuit shown in fig. 5.4. The photodiode is reverse biased, and the current generated by the photodiode is measured over a resistor that is connected in series. For a better performance an amplifier should be used, but for the purposes of these tests this crude circuit will be sufficient.

The whole setup is placed in a large dark enclosure, that can be completely closed off during the tests. This way we guarantee that no stray light reaches the detector.

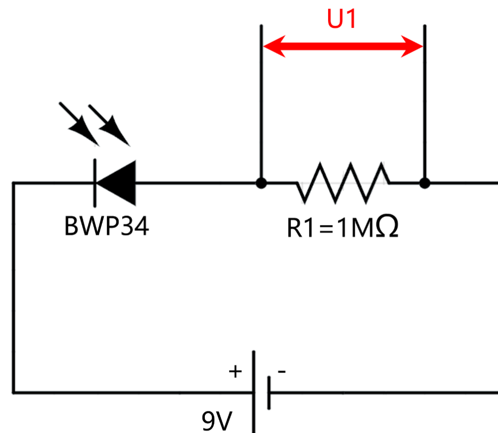

Figure 5.4: An illustration of the scanning geometry of the experimental setup

Figure 5.5

5.4. Sample droplet creation and characterization

When we take measurements on our experimental setup, it is important that we perform these measurements on a droplet of a known size, deposited on a clean wafer surface. Doing this will isolate the signal given off by the scattering droplet. Knowing the size is important for characterizing the performance of the system. It will allow us to link signal strengths to droplet sizes.

5.4.1. Droplet evaporation

As discussed in sec. 2.2, small droplets evaporate rapidly. Droplets of 35 µm will evaporate to ambient air in a matter of seconds. This means that for accurate results, it would be necessary to characterize the droplet size, and take our measurements only a fraction of a second apart. This poses quite a challenge.

To combat this problem, we decided to make our samples using sunflower oil instead of water. The optical properties of sunflower oil are close to those of water, but the evaporation rate is much lower. Observing the evaporation of sunflower oil droplets revealed a negligible evaporation rate. Approximately an hour after deposition, there was no noticeable chance to the droplets. Droplets that were left overnight, had fully dried up upon inspection. Luckily, the characterization of a droplets size, and the end of the measurement on that droplet, are only spaced out by several minutes. This means that the evaporation is negligible for our experiments.

The attenuation length of visible light in both water and sunflower oil is much larger than the length scales of the droplets. As a result, absorption in the droplet can be ignored. The refractive index of sunflower oil is slightly higher than that of water (1.46 and 1.33 respectively). This difference is not negligible, but it is in the same order of magnitude, so for a proof of concept this will suffice.

We can feed these different values for the refractive index into our model to see their effects, and use this information to extrapolate to the expected behavior of water droplets in our experimental setup.

5.4.2. Generating small droplets

Consistently applying droplets of tens of micrometers across is not a trivial task. Initially we attempted to use a microliter pipette to apply small droplets. Unfortunately these droplets were still too large.

Next, we attempted to use a plant sprayer to nebulize the oil into a fine mist. Unfortunately though, this did not work as the plant sprayer created a tightly packed jet of oil instead of a fine mist.

Then an attempt was made to deposit droplets by dipping the tip of a needle in the oil, and tapping it on the wafer surface repeatedly to deposit smaller droplets each time. Sadly however, this also did not work as

the oil did not properly adhere to the needle.

The method that worked for us was dipping a toothbrush in the oil, and subsequently rubbing it on a fine meshed metal sieve. This created a mist of oil droplets under the sieve, that slowly descended onto the wafer placed below.

Although this method worked, the droplets were tightly packed together on the wafer surface, and there was a large variety in droplet sizes. To reduce the droplet density on the wafer, and to get a more consistent droplet size, we created this droplet mist above a fan that creates a horizontal stream of air. The idea behind this is that the stream of air takes the droplets along with it. In a process similar to river sedimentation, larger droplets will fall out of the stream of air faster than smaller ones. By placing the wafer fragment further downstream, smaller droplets will be deposited on the surface. This process will also greatly reduce the density of the deposited droplets.

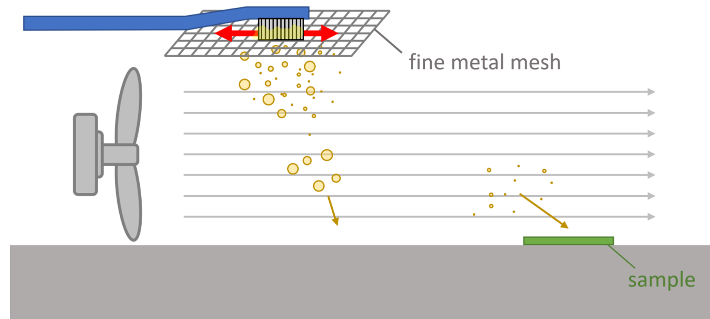

Figure 5.6: Droplets are generated by rubbing a toothbrush dipped in sunflower oil against a fine meshed metal grid. The mist of various sized droplets falls through an airflow, effectively separating the droplet sizes. The placement of the sample along the airflow will determine the droplet sizes.

5.4.3. Characterizing droplet size

For the characterization of the droplet size, a scientific camera was used with a fixed focal length lens. A contraption was built to house the camera. The camera points downwards in the contraption, at a height roughly the focal length from the table. The height of the camera can be slightly adjusted with set screws, to pull the image in focus. To illuminate the sample, a bright flashlight points at the inspection site, at a grazing angle.

The combination of camera and lens yields a pixel size of 7.5 µm. To analyze the size of a droplet, we can simply count the amount of pixels it spans. To verify this pixel size, a reticle of known dimensions is placed under the camera first. Overlaying the image of this reticle also gives us a way to quickly estimate the pixel size, without counting pixels.

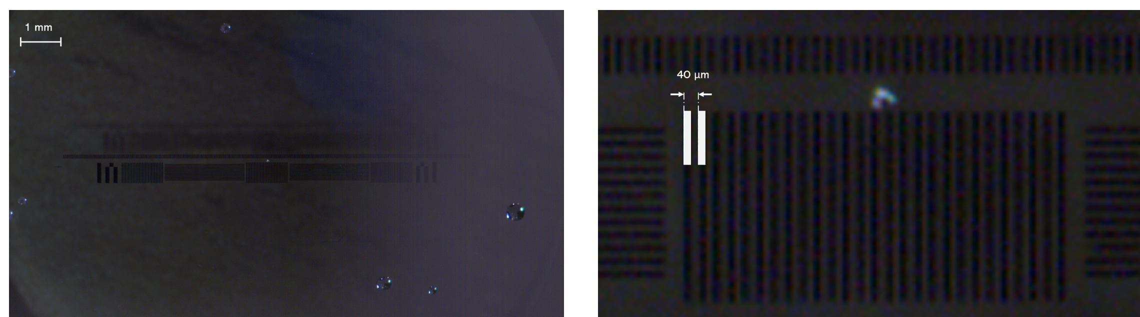

(a) Full view of the droplets deposited on the wafer surface, with the superimposed image of the reticle for scale

(b) Zooming in on the central droplet reveals a droplet size of approximately 80 µm

Figure 5.7: Droplet inspection with a scientific camera with fixed focal length lens

This setup is not ideal for characterizing droplets of around 35 µm in diameter. With a pixel size of 7.5 µm, you should in theory be able to see droplet sizes as low as 15 µm in diameter. However, as the droplets get smaller it becomes harder to distinguish droplets from defects in the wafer surface, and dust particles. Since

this experimental setup does not operate in a cleanroom, and the sample droplets are deposited on fragments of rejected wafers, these are much more commonly occurring.

Ideally a scientific camera with a smaller pixel size, or a microscope should be used to characterize the droplet sizes. However this was the best option that was readily available at that time.

5.5. Testing

The experiments have been performed on several different droplet sizes. The experiments were performed in the following steps:

1. A wafer fragment is inspected under the scientific camera to see if its sufficiently clean
2. The wafer fragment is placed on the table, at a certain distance from down the airflow to control the size of the deposited droplets
3. A toothbrush is dipped in sunflower oil, and brushed over a fine meshed metal sieve, above the start of the airflow, facing away from the wafer fragment to reduce large droplet deposition
4. After a couple of seconds, the cloud of droplets has settled, and the wafer fragment is placed under the scientific camera for inspection
5. A droplet of the desired size is selected that has sufficient separation from surrounding droplets, dust particles and scratches on the surface - an image is saved to find the exact diameter after testing.
6. The droplet is located with the naked eye, when pointing the tip of a ball point pen at the droplet, the pen tip also shows up on camera. This ensures that the correct droplet is used.
7. The wafer fragment is now placed in the experimental setup, with the selected droplet in the scan line. The laser will visually illuminate the droplet when it passes.
8. The micrometer stage is moved backwards until no signal is visible on the oscilloscope.
9. The lid of the enclosure is shut, and a measurement is saved
10. The micrometer stage is moved forwards by an increment of 12.5 µm.
11. Steps 9. and 10. are repeated until no signal is visible on the oscilloscope.

The time elapsed between depositing a droplet and finishing up its measurements were roughly 15 minutes.

5.6. Experimental findings

Six different sized droplets were tested. These droplets can be seen in fig. 5.8 The measurements that are taken are a current as a function of time, for each 12.5 µm slice in the cross-scan direction. Because we know the dimensions of the scan line, and the frequency of the galvanometer scanner, we can convert these measurements to a raster scanned image of the surface.

5.6.1. Measurement results

The measurements that were taken can be seen in fig. 5.9. Each subfigure contains a 3D-view of the scanned profile with the scan- and cross-scan dimensions on the x- and y axes, and the signal on the z axis. Additionally, each subfigure contains a colormap with the cross-scan- and scan-dimensions on the x- and y axes respectively.

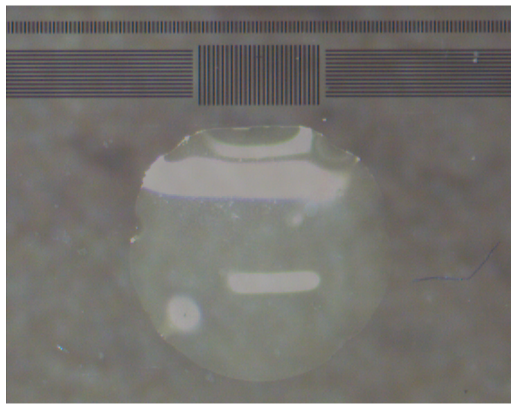

(a) Measurement 1 - 2164 µm

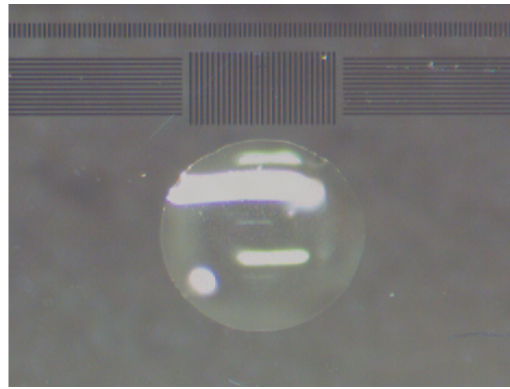

(b) Measurement 2 - 1358 µm

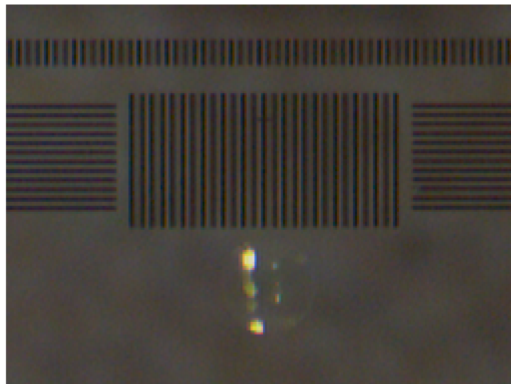

(c) Measurement 3 - 368 µm

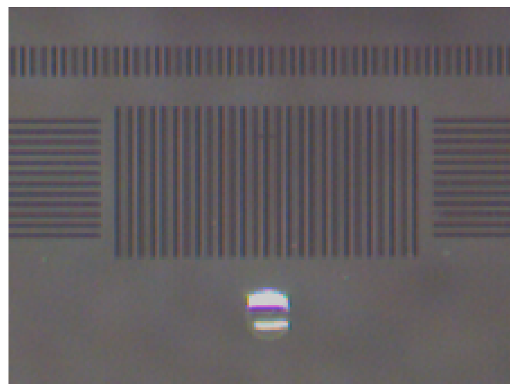

(d) Measurement 4 - 180 µm

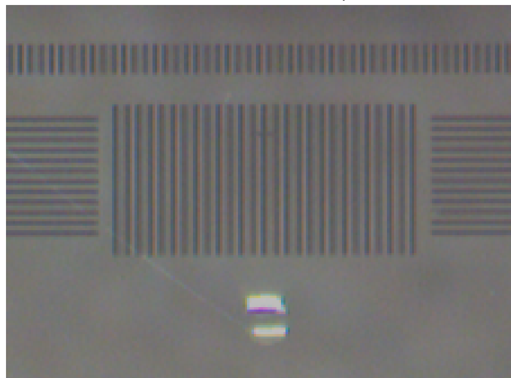

(e) Measurement 5 - 173 µm

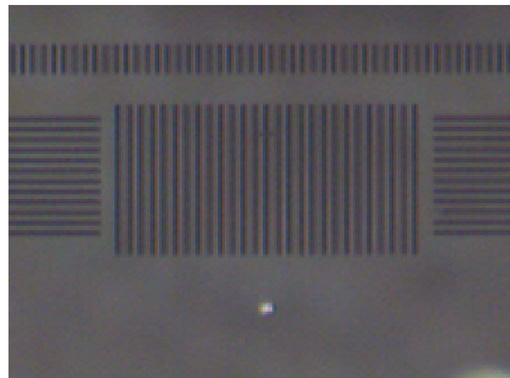

(f) Measurement 6 - 49 µm

Figure 5.8: The different droplets that were measured on the experimental setup

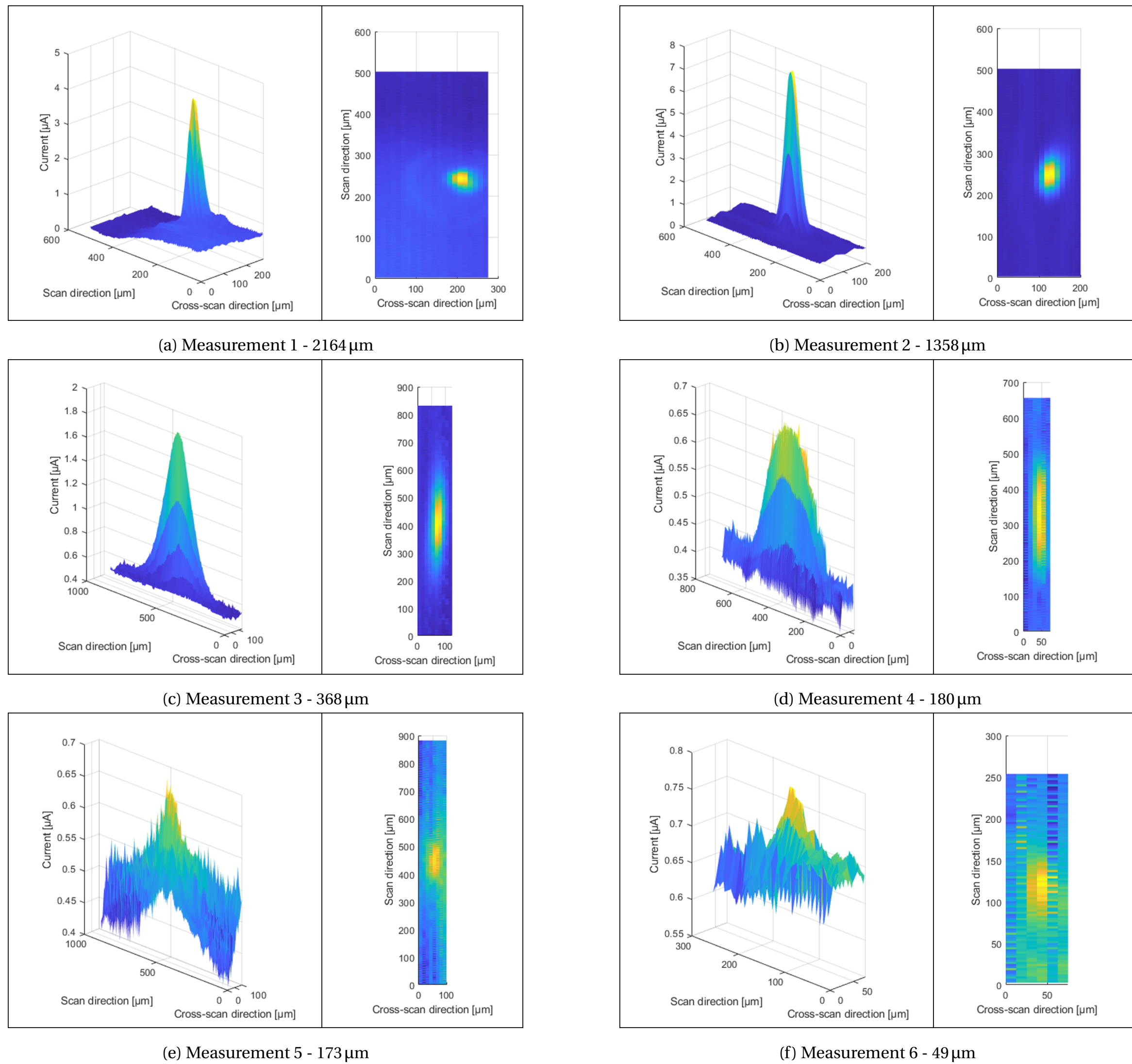

(a) Measurement 1 - 2164 µm

(b) Measurement 2 - 1358 µm

(c) Measurement 3 - 368 µm

(d) Measurement 4 - 180 µm

(e) Measurement 5 - 173 µm

(f) Measurement 6 - 49 µm

Figure 5.9

5.6.2. Measurement results interpretation

The first observation we can make is that the measurements show a distinct peak where the droplet is located, which means our detection principle works. The peaks are very narrow compared to the droplet size, especially for the larger droplets. In the cross-scan direction the width of the peaks seems to be completely insensitive to droplet size. This indicates that the droplets are flat. Our model assumes a perfectly hemispherical droplet, the flatter the droplets get the narrower the response will be. In the scan direction however the droplets seem to correspond relatively well to their respective droplet sizes - except for measurement 4. It seems like the wrong droplet is inspected - since the measurement shows a response over 300 µm wide - although the droplet itself should only be 180 µm in diameter. It is not unlikely that two droplets got mixed up - since after inspecting the droplets with the camera, the droplet must be tracked with the naked eye while the sample is placed under the scanner. The smaller the droplets get the more noise seems to influence the measurements. Even for the smallest droplets the peak is visibly distinguishable from the noise - however the noise is much higher than predicted in our model. This might be due to 1) the high value resistor used in the diode circuit, 2) improper shielding of the circuit, while the high voltage power supply is turned on in very close proximity, 3) improper grounding; there seemed to be a grounding issue at first - after which the circuit was grounded to the optical cage system. However this might have been insufficient, or lastly due to 4) the crude circuit. The circuit did not use any filters to limit the bandwidth - which can increase the noise. It is unclear if the oscilloscope has something similar built in. When we look closely at the first two measurements, a second ring is revealed. At first this was thought to be an artifact of the bowed scan trajectory on the

obstruction strip - partially leaking past at the extremities of the scan line. However upon closer inspection we think it is a scattering signal from the edge of the droplet.

We can see that the amplitude of the signal for the larger droplets increases, however we are not able to say by how much, since the spot is much smaller than the droplet size. Our model relies on the signal strength to vary with the square of the droplet sizes, when the spot is much larger than the droplet. Because of the small spot size in our experimental setup, it is difficult to investigate if this relation holds. Additionally more measurements should be performed on similar sized droplets to find out if the response of same-sized droplets varies. In this report the assumption was made that droplet shapes do not vary significantly at the length scales we are interested in - however this should be experimentally validated.

The experimental results gave us some nice insights in the scattering behavior of droplets. The narrow peaks indicate that the large majority of the scattered light we measure is generated in a very small area on the droplet surface. However in hindsight this was not a very good experiment to validate the design. Measuring with a larger spot would have been better to validate the model.

6 Conclusion & recommendations

In this report the design and validation of a surface inspection tool for rapid water detection on a silicon wafer is presented. The surface inspection tool is part of the proposed redesign of the Temperature Stabilization Unit (TSU) of VDL-ETGs Atmospheric Wafer Handler (AWH). The redesign utilizes water as its thermal conduction medium instead of air. Before the wafer continues to the lithography machine, the water must be removed and the wafer must be inspected. The subgoals that were set up for this project are the following: 1) Set up the system requirements and wishes, 2) Generate feasible concepts, and make a justified selection, 3) Make a design based on first principles, 4) Build and test a prototype, 5) Finalize a detailed design and test its performance. The conclusion is structured in accordance with these subgoals. Subsequently some recommendations for further research are elaborated.

6.1. Conclusion

A thorough requirement study was performed, to minimize the risk of spending time and energy on a solution that turns out to be inherently flawed, or on problems that turn out to be irrelevant. The cycle time of the current AWH is 17 seconds, 10 seconds of which constitute the thermal conditioning time. Although some other actions (centering and rotation to notch) are performed simultaneously with the thermal conditioning, there is a three second window where the AWH uniquely performs thermal conditioning. Reducing the conditioning time by three seconds will as a result directly increases the throughput of the machine by 21.4%. Achieving this three second conditioning time reduction requires the inspection tool to perform its measurement in approximately two seconds. The confidentiality that is ubiquitous in the semiconductor industry prevented us from finding some key specifications of lithography processes, such as commonly used coatings, and allowable contamination levels of the backside of wafers. To guarantee that water contamination does not cause any issues further up in the machine, we selected the lower bound of our detection range such that undetected droplets fully evaporate before the wafer moves to the next process step. From literature we derived that surface deposited droplets with diameters of 35 μm evaporate in less than 4 seconds, which is the time it takes for the AWH to unload a wafer. A false positive measurement (type 2 error) is not critical, but it will add an additional measurement cycle, causing an increase in conditioning time. To assure that the total throughput is affected by less than one percent as a result of type 2 errors, the false positive rate must remain below one event per 15 wafers. False negative measurements (type 1 error) are critical, since they cause a droplet to pass undetected. Type 1 errors may only occur roughly once every 24 hours of operation. This means that the false negative rate must be lower than one event per 6200 wafers. The droplets must be detected, however quantifying their location, shape or size is not required for the system to be fully functional. Lastly, the inspection may not increase the average wafer temperature by more than 3 mK, and may not induce temperature non-uniformities larger than 1 mK within a distance of 100 mm.

The concept generation phase was tackled with a ground up approach. First the feasibility of different detection principles was investigated. Both common detection principles (bright field imaging, dark field imaging, interferometry, acoustic imaging) and more niche detection principles (polarization imaging, absorption imaging) were evaluated. Acoustic imaging was rejected due to insufficient spatial resolution, and the difficulty of separating the signal (droplet) from the background (wafer). Optical imaging with dark field illumina-

tion is deemed the most suitable method for this specific problem, since it can achieve much higher contrast than bright field, polarization and absorption imaging, and due to its low sensitivity to wafer displacement compared to interferometry. Several camera- and scanner concepts are generated, which can be seen in fig. 3.4a, 3.4b and 3.5. As summarized in tab. 3.1, the concepts are judged on three performance criteria; 1) discriminative power (i.e. how well is the system able to distinguish positive and negative measurements), 2) measurement time and 3) effect on wafer temperature. The synchronous dark-field flying spot scanner is selected as the most promising concept for this problem. As a result of the scanner geometry, the power of the light reaching the detector is only a function of droplet size and shape - and thus independent of droplet location. This allows us to directly link a signal strength to a droplet size, without the need for complicated signal processing. Additionally, the small laser spot that is used for inspection yields a high signal-to-noise ratio and a minimal background signal when compared to other illumination techniques. Reaching a similar discriminative power with other illumination techniques will require more light, and will thus have a larger effect on wafer temperature.

The conceptual design works in the following way: Raster scanning is achieved by combining the fast scanning motion (scan direction) of a rotating polygon mirror, which generates scan lines pointing radially outwards from the center of the wafer, with the slow scanning motion of the rotating wafer (cross-scan direction) to separate these scan lines. This is illustrated in fig. 4.5. The beam is incident on the polygon under an angle w.r.t. the plane of rotation of the polygon. The resulting deflection pattern of the beam follows a conical section, which generates scan lines on the wafer surface in the shape of a circular arc, as illustrated in fig. 4.4. To achieve synchronous scanning, a cylindrical mirror is placed behind the scan line, such that the scan line and the cylindrical mirror are concentric. Together, the wafer surface and the cylindrical mirror function in a similar fashion to a corner reflector - effectively reflecting the beam back in the same direction from which it originated, only with some vertical offset. The returning beam is then incident on the rotating polygon mirror for a second time, which effectively reverses the scanning motion - making the returning beam stationary after reflection. To achieve dark-field illumination, a small circular obstruction is placed in the optical path of the returning beam, preventing the direct beam from reaching the detector. The scattered light that grazes past the obstruction is then focused on the detector, generating the signal.

For first principles design we are interested in finding a design with the desired 1) measurement time, 2) effect on wafer temperature and 3) type 1 and 2 error rates. To meet the measurement time requirement, the measurement time has simply been set to 2 seconds. Reducing the measurement time any further would not necessarily be beneficial for the system, and having more time available for measurement alleviates some pressure on the rest of the design. Next, the effect on wafer temperature is evaluated. The amount of thermal energy added to the wafer is a function of laser power and exposure time. With the chosen illumination pattern, the temperature non-uniformity constraint is critical over the average temperature constraint. A total of 66.7 mJ of thermal energy must be added to the wafer to break the non-uniformity constraint. With the absorption of silicon and the exposure time of two seconds this yields a maximum laser power of 53 mW. Lastly, the error rates are evaluated. As illustrated in fig. 4.1, the signal strength (i.e. expected signal for a 35 μm diameter droplet) and signal variation (i.e. non-stochastic variation as a result of errors such as wafer deformation and droplet location within spot) are used to find the noise contribution that is required for a type 1 or type 2 error to occur. Comparing the expected noise power with the noise contribution that is required for an error, allows us to find the rate at which the respective errors will occur. To find the signal strength, a ray optics simulation is performed in Matlab to find the scattering profile of a droplet - and the geometry of the scanner is evaluated to find the FOV from the droplet to the detector. Although this simulation ignores effects of absorption and diffraction, and assumes perfectly hemispherical droplets deposited on an ideal reflective surface, it is deemed sufficient to get an estimate of the scattering profile. The accuracy of this simulation is not very important, since the results are only used to find a functional design - eventually the surface inspection tool will be fine tuned through calibration. To find the signal variation we evaluate effects that can 1) change the illumination a droplet experiences, 2) change the FOV to the detector w.r.t. the optical axis or 3) change the scattering profile. The illumination a droplet experiences is determined by its location in the laser spot during measurement. The worst-case location of a droplet within the spot is a function of spot size, scan line separation, sample rate and scan line error induced by facet-to-facet angle errors of the polygon. In addition, errors that introduce a defocus of the beam, such as wafer warp, can increase the illumination variation even further. The FOV to the detector w.r.t. the optical axis changes for different positions on the scan line, however these effects can be easily corrected for since they are predictable. The scattering profile can be affected by droplet shape. However in our observations we see that there is less variation in droplet

shapes the smaller droplets become. The assumption is made that for the droplet sizes we are interested in, the variation in scattering profile between different droplets on the same wafer is negligible. The hydrophobicity of the wafer, which can change with different coatings, is however expected to have a significant effect on droplet shape - and thus the scattering profile. This can however be corrected for through calibration. All of these calculations are incorporated in a parametric design tool that is created in Excel. This design tool takes inputs such as measurement time, spot size, and scanner geometry - and translates them to an expected performance. The design parameters were tweaked until a desirable design was found. A summary this design can be seen in tab. 6.1. A volume design is created in SolidWorks to see if the design meets the build volume requirements. Folding mirrors are added to make the design more compact. The design now has the added bonus that it fits in a section of the build volume specified for the current TSU - allowing the redesign to be fitted with minimal adjustments to the current AWH layout.

property	**value**	**requirement**
minimum beam waist ($2w_0$)	100 µm	
bandwidth	17.1 MHz	
incident angle	11.3°	
radial scan distance	90 mm	
pixel size	25 × 180 µm	
polygon facet size	25 × 30 mm	
polygon facet count	8	
polygon rotation speed	19600 rpm	
polygon duty cycle	0.8	
cylindrical mirror offset	40 mm	
obstruction diameter	11 mm	
signal power	8.8 nW	
signal variation	< 15.8%	
measurement time	2 s	≤ 2s
S/N rate	28.5 dB	≥ 26.4 dB
wafer heating	43.8 mJ	≤ 66.7 mJ

Table 6.1: Summary of the properties of the design that was found

To validate the design an experimental setup was built. This setup uses a simplified version of the design, where the cylindrical mirror has been removed, and the circular obstruction is replaced by an obstruction strip. Since water droplets evaporate rapidly, sunflower oil droplets are investigated instead of water. The optical properties of sunflower oil are comparable to those of water - and the evaporation rate is much lower. A spot size of 40 µm was chosen to better quantify the scattering behavior of the droplets. Fig. 5.3 shows an illustration of the test setup, and the test procedure is detailed in sec. 5.5. Six different droplets are evaluated, with the respective diameters of 2164, 1358, 368, 180, 173 and 49 µm. Although we are mainly interested in droplets in the range of 35 µm, our camera is not suitable to identify droplets to that size properly. The results of these measurements can be seen in fig. 5.9. As expected the measurements show a peak where the droplet is located. As is most clearly visible from the largest two droplet measurements, the large majority of the measured scattering originates from a small area on the droplet. The width of the peaks in the cross-scan direction is approximately equal to the spot size in the cross-scan direction, and seems to be independent of droplet size. The width of the peaks in the scan direction seems to be approximately equal to the droplet size for the smaller droplets. However for the largest two measurements this does not hold. The peaks are visibly distinguishable from the noise, however the measured noise level is significantly higher than the noise level predicted by the model. This is attributed to either 1) poor shielding, 2) poor grounding or 3) a lack of bandwidth limiting circuitry. Our model relies on the signal strength varying by the square of the droplet sizes. This is only assumed to apply when the spot is much larger than the droplets. Because the chosen spot was only 40 µm it is difficult to investigate if this relation holds. These experimental results contain valuable information, however the results are not sufficient to fully validate the design. More experimental work is required to show 1) if the signal amplitude scales with the area of the droplets, 2) if there is significant variation in the response of droplets of the same size and 3) if its possible to bring the noise levels down

To summarize, a requirements study was performed, concepts were generated, and the most feasible con-

cept was selected. A design was found that meets the performance criteria based on first principles, and an experimental setup was constructed, on which tests were performed. The measurement results were insightful, however not sufficient to fully validate the design. Lastly, making the detailed design and testing its performance did not fit in the timetable of the research, so this is saved for future research. This report shows a solid foundation for a surface inspection tool design. The powerful parametric design tool gives an easy way to tweak the design, or to add in new important factors that show up in future research.

6.2. Recommendations

Due to time limitations the design study did not reach its ultimate conclusion: a physical, functional surface inspection tool that meets the requirements. To guide further development of this surface inspection tool some recommendations are listed.

The first recommendation is to improve the experimental setup by 1) choosing a larger spot size and by 2) improving the resolution of the pre-measurement inspection, allowing smaller droplets to be selected for measurement. With a larger spot size to droplet size ratio it is possible to do measurements to verify the calculated signal amplitude. Additionally, this will allow for measurements to investigate the relation between droplet size and signal ratio. Currently our calculations rely on the assumption that signal amplitude is proportional to the square of the droplet diameter (in situations where the spot is much larger than the droplet). This relation plays a big role in the error rate calculations, and should be experimentally validated.

The next recommendation is to investigate ways to reduce the noise level. The noise level in the measurements is much higher than predicted in our model. We currently believe that this is due to the large value resistor used in the circuit, improper grounding or due to the poor shielding of the circuit, which is placed directly next to a high voltage power supply. With this large noise value, the system will not be able to meet the error rate requirements.

Penultimately, we recommend performing multiple measurements of similar sized droplets to characterize the variation in droplet shapes. Droplet shape is currently neglected as a factor influencing signal variation, however the measurement results indicate that the droplet shapes do indeed vary.

Finally we recommend investigating the possibility of reducing the wafer warp. During measurement, the wafer is only fixated at the center by the P-chuck. The lack of fixation of the wafer allows the wafer to be warped, causing both positional and angular errors of the wafer. These errors are a large contributor of various errors in the system. Reducing this wafer warp will make the design a lot more efficient.

Bibliography

[1] Bright field and dark field lighting. URL https://www.microscan.com/en-us/resources/know-your-tech/bright-field-and-dark-field-lighting.

[2] Introduction to polarization. URL https://www.edmundoptics.com/knowledge-center/application-notes/optics/introduction-to-polarization/.

[3] Electromagnetic absorption by water, Feb 2021. URL https://en.wikipedia.org/wiki/Electromagnetic_absorption_by_water.

[4] ASML. EPS TSU Redesign MK6 for XT-extensions, D0000293099-00-EPS-001, April 2014.

[5] D. E. Aspnes and A. A. Studna. Dielectric functions and optical parameters of si, ge, gap, gaas, gasb, inp, inas, and insb from 1.5 to 6.0 ev. *Phys. Rev. B*, 27:985–1009, Jan 1983. doi: 10.1103/PhysRevB.27.985. URL https://link.aps.org/doi/10.1103/PhysRevB.27.985.

[6] Peter J. de Groot. A review of selected topics in interferometric optical metrology.

[7] M. Ehrhardt, C. Degel, F. J. Becker, L. Peter, H. Hewener, H. Fonfara, M. Fournelle, and S. Tretbar. Comparison of different short-range sonar systems on real structures and objects. In *OCEANS 2017 - Aberdeen*, pages 1–6, 2017. doi: 10.1109/OCEANSE.2017.8084758.

[8] Peng Fei Gao, Gang Lei, and Cheng Zhi Huang. Dark-field microscopy: Recent advances in accurate analysis and emerging applications. *Analytical Chemistry*, 93(11):4707–4726, 2021. doi: 10.1021/acs.analchem.0c04390. URL https://doi.org/10.1021/acs.analchem.0c04390. PMID: 33620210.

[9] Y. S. Huang and M. S. Young. An accurate ultrasonic distance measurement system with self temperature compensation. *Instrumentation Science & Technology*, 37(1):124–133, 2009. doi: 10.1080/10739140802584780. URL https://doi.org/10.1080/10739140802584780.

[10] Rongqing Hui. *Introduction to Fiber-Optic Communications*. Academic Press, 2020.

[11] Junjie Li*, Weixia Zhang*, Ting-Fung Chung, Mikhail N Slipchenko, Yong P Chen, Ji-Xin Cheng, and Chen Yang. Highly sensitive transient absorption imaging of graphene and graphene oxide in living cells and circulating blood. *Scientific reports*, 5:12394, 2015.

[12] Pedro Lilienfeld. Optical detection of particle contamination on surfaces: A review. *Aerosol Science and Technology*, 5(2):145–165, 1986. doi: 10.1080/02786828608959085. URL https://doi.org/10.1080/02786828608959085.

[13] G.F. Marshall and G.E. Stutz, editors. *Handbook of Optical and Laser Scanning*. CRC Press, second edition edition, 2012.

[14] Zeng Nan, Jiang Xiaoyu, Gao Qiang, He Yonghong, and Ma Hui. Linear polarization difference imaging and its potential applications. *Appl. Opt.*, 48(35):6734–6739, Dec 2009. doi: 10.1364/AO.48.006734. URL http://ao.osa.org/abstract.cfm?URI=ao-48-35-6734.

[15] S. Rahmann and N. Canterakis. Reconstruction of specular surfaces using polarization imaging. 1:I–I, 2001. doi: 10.1109/CVPR.2001.990468.

[16] G. Reinaudi, T. Lahaye, Z. Wang, and D. Guéry-Odelin. Strong saturation absorption imaging of dense clouds of ultracold atoms. *Opt. Lett.*, 32(21):3143–3145, Nov 2007. doi: 10.1364/OL.32.003143. URL http://ol.osa.org/abstract.cfm?URI=ol-32-21-3143.

[17] S. Roy, K. Ushakova, Q. van den Berg, S. F. Pereira, and H. P. Urbach. Radially polarized light for detection and nanolocalization of dielectric particles on a planar substrate. *Phys. Rev. Lett.*, 114:103903, Mar 2015. doi: 10.1103/PhysRevLett.114.103903. URL https://link.aps.org/doi/10.1103/PhysRevLett.114.103903.

[18] E. L. Talbot, A. Berson, P. S. Brown, and C. D. Bain. Evaporation of picoliter droplets on surfaces with a range of wettabilities and thermal conductivities. *Phys. Rev. E*, 85:061604, Jun 2012. doi: 10.1103/PhysRevE.85.061604. URL https://link.aps.org/doi/10.1103/PhysRevE.85.061604.

[19] Akio Yazaki, Chanju Kim, Jacky Chan, Ata Mahjoubfar, Keisuke Goda, Masahiro Watanabe, and Bahram Jalali. Ultrafast dark-field surface inspection with hybrid-dispersion laser scanning. *Applied Physics Letters*, 104(25):251106, 2014. doi: 10.1063/1.4885147. URL https://aip.scitation.org/doi/abs/10.1063/1.4885147.

[20] Tao Yu, Bo Tian, and Weiwei Cai. Development of a beam optimization method for absorption-based tomography. *Opt. Express*, 25(6):5982–5999, Mar 2017. doi: 10.1364/OE.25.005982. URL http://www.opticsexpress.org/abstract.cfm?URI=oe-25-6-5982.